

METAL / SEMICONDUCTOR CONTACT RESISTIVITY AND ITS DETERMINATION FROM CONTACT RESISTANCE MEASUREMENTS

Andrea SCORZONI and Manuela FINETTI

CNR, Istituto LAMEL, via Castagnoli 1, 40126 Bologna, Italy

Received 12 May 1988; in final form 28 June 1988



1988

NORTH-HOLLAND – AMSTERDAM

Contents

1. Introduction	82
2. Contact resistivity and contact resistance	82
2.1. Physical model of the contact interface	82
2.2. Practical metal/semiconductor interfaces	84
2.3. Vertical and horizontal current flow	87
2.4. Theoretical models	88
2.5. Scaling theory and generalized simulation curves	92
2.6. Test structures for the extraction of the contact resistivity from contact resistance measurements	93
3. Transmission line resistors	95
3.1. The transmission line tap resistor (TLTR)	95
3.2. Parasitic effects	98
3.3. Electrical characterization of conventional metal systems on silicon	102
3.4. The circular transmission line resistor (CTLR)	106
4. Four-terminal single-contact Kelvin resistors: the cross Kelvin resistor (CKR)	108
4.1. One-dimensional model and first experimental results	108
4.2. Two-dimensional current flow	110
4.3. Comparison between D- and L-resistors	115
4.4. Sheet resistance modification effects	117
4.5. Analytical models	118
4.6. Optimization of the test structure	120
5. Four-terminal single-contact Kelvin resistors: the contact end resistor (CER)	120
5.1. Description of the test structure and first experimental results	120
5.2. Two-dimensional current flow	121
5.3. Misalignment effects	121
5.4. Generalized extraction curves and sheet resistance modification effects	123
6. The six-terminal Kelvin resistor	123
6.1. Description of the test structure	123
6.2. Misalignment effects	125
7. New test structures	129
7.1. The self-aligned contact end resistor (SCER)	129
7.2. The self-aligned six-terminal cross Kelvin resistor (SKR)	130
7.3. The circular resistor (CR)	131
8. Contact resistance in VLSI contacts	132
8.1. Contact resistance and scaling	132
8.2. Contact resistivity and reliability	133
9. Conclusions	134
Acknowledgements	134
References	135

METAL/SEMICONDUCTOR CONTACT RESISTIVITY AND ITS DETERMINATION FROM CONTACT RESISTANCE MEASUREMENTS

Andrea SCORZONI ¹ and Manuela FINETTI ²

CNR, Istituto LAMEL, via Castagnoli 1, 40126 Bologna, Italy

Received 12 May 1988; in final form 28 June 1988

In this paper the relation between contact resistivity and contact resistance is examined. The most widely used methods for contact resistance measurements and extraction of the contact resistivity are presented. Different types of approach, aimed to improve the accuracy and sensitivity of the various techniques are then extensively discussed. In each case, applications to practical contacts, mainly metal systems on heavily doped silicon, are also shown. Finally, the impact of a low contact resistivity on contact performance and reliability is mentioned.

¹ Also with DEIS, viale Risorgimento 2, 40126 Bologna, Italy.

² Present address: CEE, Rue de la Loi 200, A25-4/8, 1049 Brussels, Belgium.

1. Introduction

The contact resistivity, ρ_c ^{#1}, is considered as an important figure of merit to evaluate the quality of an ohmic contact. It is in fact one of the basic parameters by which different metal systems or metal preparation procedures are typically examined, compared and selected. Moreover, ρ_c can give information on the surface doping level in the semiconductor, hence providing useful insights into the contact formation mechanisms, or can be monitored to test the contact stability and reliability.

It frequently happens that the electrical properties of metallization systems are compared among different authors, only a few of them indicating the precautions taken to assure an accurate evaluation of ρ_c , some of them not even specifying the measuring method being applied.

In our opinion, it should be realized that a correct evaluation of ρ_c is not simple at all, specially for ρ_c values less than $10^{-6} \Omega \text{ cm}^2$ like the ones typically required in modern integrated circuit technology. It is not a useless task either, as the large amount of papers on this topic seems to confirm.

It could be argued that the determination of the contact resistance, R_c , alone is sufficient to evaluate the contact quality. However, this is only partially true, since the information derivable from R_c is of limited benefit, in the comparison of different metal systems as well as in the analysis of the metal formation mechanisms, R_c being strongly dependent on the geometrical characteristics of the particular contact structure under test.

Moreover, it should be pointed out that an accurate analysis of the electrical parameters, like contact resistivity and sheet resistance below the contact, and the use of proper simulation tools, allows the prediction of the contact resistance for any type of geometry, down to submicron dimensions, which is of increasing practical interest in the design of VLSI and ULSI contacts.

In this paper, after a short description of the metal/semiconductor interface, from both theoretical and experimental points of view, the relation between contact resistivity and contact resistance is examined. The most widely used methods for contact resistance measurements and extraction of the contact resistivity are presented. Different types of approach, aimed to improve the accuracy and sensitivity of the various techniques are then extensively discussed. In each case, applications to practical contacts, mainly metal systems on heavily doped silicon, are also shown. Finally, the impact of a low contact resistivity on contact performance and reliability is mentioned.

2. Contact resistivity and contact resistance

2.1. Physical model of the contact interface

A comprehensive analysis of the fundamental transport properties in metal/semiconductor contacts can be found in refs. [1–5]. In this section we will restrict ourselves to a brief description of the mechanisms of current transport and their dependence on temperature, barrier height, doping concentration, and presence of graded band gap layers.

In the case of metal/silicon contacts, the conduction properties are determined essentially

^{#1} Also known as “specific contact resistivity”, “specific contact resistance”, “specific interface resistance”, “specific resistance” and even “contact resistance”.

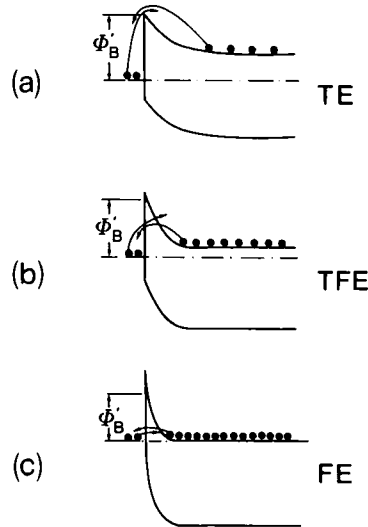


Fig. 1. Conduction mechanisms for metal/n-semiconductor contacts as a function of the barrier height and width. The barrier height is reduced from its original value ϕ_B to ϕ'_B as a result of the image force lowering. (a) Thermionic emission; (b) thermionic-field emission; (c) field emission.

by the width of the depletion region formed at the interface, which gives rise to the following two fundamental mechanisms:

(1) Thermionic emission (TE), occurring in the case of a depletion region so wide that the only way for electrons to jump the potential barrier is by emission over its maximum (fig. 1a). The barrier height is reduced from its original value ϕ_B to ϕ'_B as a result of image force barrier lowering.

(2) Field emission (FE), consisting in carrier tunnelling through the potential barrier. This mechanism, which is the preferred transport mode in ohmic contacts, takes place when the depletion layer is sufficiently narrow, as a consequence of the high doping concentration in the semiconductor (fig. 1c).

The relative magnitude of the two transport components, which depends on barrier height, temperature, doping concentration, charge carrier effective mass and dielectric constant, determines the rectifying or ohmic properties of the contact. A useful parameter to this purpose is the ratio kT/E_{00} , where the energy E_{00} is related to the probability of tunnelling and is defined as

$$E_{00} = (q\hbar/2)(N/m^*\epsilon)^{1/2}, \quad (2.1)$$

where q is the electronic charge, \hbar the reduced Planck constant, N the dopant concentration, m^* the effective mass of the tunnelling carriers and ϵ the dielectric constant of the semiconductor.

As mentioned above, the value of the ratio kT/E_{00} is an indication of the predominance of one mechanism with respect to the other. For $kT/E_{00} \gg 1$, for example, thermionic emission is the dominant contribution and the contact behaves as a Schottky barrier. For $kT/E_{00} \ll 1$, at very high doping levels or very low temperatures, field emission prevails and the contact is ohmic. When $kT/E_{00} \approx 1$, a mixed-mode transport takes place, referred to as thermionic-field emission (TFE). In this case the current flow is mostly contributed by carriers with some thermal energy, tunnelling at the midsection of the barrier (fig. 1b).

The ohmic properties of the contacts are characterized by the contact resistivity, defined as

$$\rho_c = [(\partial J / \partial V)_{V=0}]^{-1}, \quad (2.2)$$

where J is the local current density flowing across the contact, and V the local potential drop across the interface.

Knowing the basic transport equations, theoretical expressions for ρ_c have been derived for the different regimes of current flow [1,2,4], showing the following dependence on temperature, barrier height and tunnelling probability

$$\rho_c \propto \exp(q\phi'_B/kT) \quad (\text{TE}), \quad (2.3a)$$

$$\rho_c \propto \exp\left[\frac{q\phi'_B}{E_{00} \coth(E_{00}/kT)}\right] \quad (\text{TFE}), \quad (2.3b)$$

$$\rho_c \propto \exp(q\phi'_B/E_{00}) \quad (\text{FE}). \quad (2.3c)$$

Fig. 2 shows theoretical curves of ρ_c versus dopant concentration N for different values of barrier height on p-type and n-type $\langle 111 \rangle$ oriented silicon.

By neglecting the influence of temperature and tunnelling effective mass it is evident from eqs. (2.3) that two ways, basically, are available for achieving ohmic contacts. From a technological point of view, the most used approach consists in increasing the doping concentration in the semiconductor. In this way, even a high barrier contact will become ohmic, because of the increased probability of quantum-mechanical tunnelling through the potential barrier.

A second approach consists in employing, at direct contact with the semiconductor, a metal of low barrier height. However, it must be observed that, by increasing the doping level, differences in barrier height become less important.

The tunnelling mechanism through the barrier between metal and crystalline semiconductor has been extensively invoked in the past to explain also the ohmic behaviour of contacts to III-V compounds [4,6-9]. Furthermore, in this case, the barrier height is essentially independent of the particular metal in contact with the semiconductor. This was attributed to surface states [10,11] or to chemical reactivity at the interface [12], in particular to microclusters resulting from oxygen contamination or metal-semiconductor reactions [13].

Other models have been presented in order to explain the formation of ohmic contacts that cannot be based on highly doped contact layers, such as indium contacts on GaAs and GaSb [5,14-16]. Sebestyen [5] has suggested that ohmic behaviour could be obtained from tunnelling between closely-spaced localized states in the disordered interface. Woodall et al. [14] suggested that, due to the fact that for InAs surfaces Fermi level pinning occurs at or in the conduction band, a graded heterojunction should provide an ohmic contact with low contact resistivity. Finally, some recent Raman scattering studies by Krillow and Chung [17] indicate that heavy doping is not present in Au-Ge-Ni contacts to GaAs, supporting Sebestyen's model, and Farrow et al. [18] interpreted their Raman data as indicating a lower barrier height due to surface state reduction.

2.2. Practical metal / semiconductor interfaces

Metal/semiconductor ohmic contacts can be basically classified into three categories shown in figs. 3a, 3b and 3c.

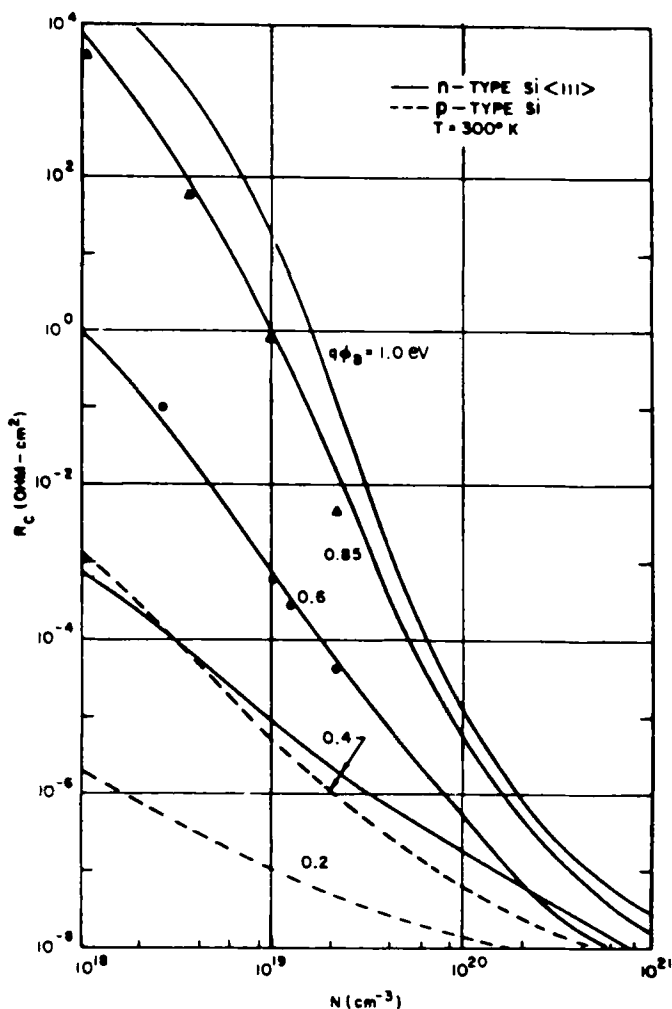


Fig. 2. Theoretical contact resistivity at 300 K for n-type, $\langle 111 \rangle$ oriented (solid lines) and p-type (dotted lines) silicon. The solid circles are experimental results of Al/Si and Mo/Si barriers ($\phi_B = 0.6$ eV), and triangles for PtSi/Si barriers ($\phi_B = 0.85$ eV). From ref. [2].

The case of unreacted contact, characterized by the sharp interface between metal and semiconductor, is shown in fig. 3a. A typical example for this type of contact is represented by a film of TiN directly in contact to Si. TiN is in fact well known as a thermally stable compound, and it is one of the most attractive diffusion barriers in integrated circuit technology [19]. An important problem associated to this, and similar inert materials is that the

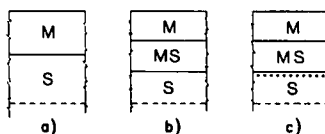


Fig. 3. Schematic diagram of possible metal (M) and semiconductor (S) ohmic contact configurations: (a) unreacted contacts; (b) reacted contacts; (c) reacted contacts with a dopant element in the metallization system.

semiconductor surface treatment, before metal deposition, assumes a fundamental role in determining the contact quality. Residual oxides or contaminants between metal and substrate can in fact cause ρ_c values considerably higher than the ones predicted by the theory [20,21]. For example, in ref. [21] values of ρ_c of $\sim 2.8 \times 10^{-4}$ and $\sim 1.5 \times 10^{-5} \Omega \text{ cm}^2$ were determined on solar cell type Si, for TiN/p⁺-Si (about 10^{20} boron atoms/cm³) and TiN/n⁺-Si (about 2×10^{20} phosphorus atoms/cm³) metallization schemes. Furthermore, surface damage induced during the metal deposition in the highly doped layer, and appearing as electrically active traps, can appreciably affect the resulting electrical properties of the contact [22].

Reactions of metals with semiconductors are, in many cases, not only unavoidable, but even desirable, since they lead to improved thermal stability and superior electrical performance. Typical examples of reacted contacts (fig. 3b) are the transition-metal silicides. These films have been extensively investigated as low-resistive, reproducible metal systems on heavily doped silicon. The electrical properties of several silicide/silicon interfaces have been presented in the literature by different authors, reporting values of contact resistivity typically in the range $10^{-8} < \rho_c < 10^{-6} \Omega \text{ cm}^2$ [23–40]. In particular, Pd, Pt, Ti, Ta and Mo silicides were extensively studied for applications in VLSI.

For the purpose of this paper, it should be mentioned that dopant redistribution, the so-called “snow-plow” effect, can occur during silicide formation [41–45]. From the reduction of the contact resistivity before Pd₂Si formation up to complete reaction, Ohdomari et al. [26] monitored the piling-up of arsenic at the Pd₂Si/n⁺-Si interface, and determined the fraction of electrically active dopant out of the total redistributed.

Finally fig. 3c illustrates the case of contacting metals containing dopant elements. Contacts of this type are widely used on GaAs and can be formed by liquid- or solid-phase reactions. In the first case, during heating, one or more metal components are molten, and the surfacial layer of the semiconductor is dissolved in the melt. On cooling down, the dopant segregates from the melt, together with the solidifying semiconductor, thus enhancing the doping level near the surface. Gold is preferably used as the base metal in these alloyed contacts. Zn, Be, sometimes Mg, are typically chosen as acceptors for contacts to p-type GaAs. For the n-type, Te, Se, Si, Ge and Sn can be used as donors. Currently, the most widely used ohmic contacts to n-type III–V compounds are based on the Au–Ge–Ni system. Very low contact resistivities ($\sim 10^{-6} \Omega \text{ cm}^2$) have been achieved with this system. However, the poor interface morphology due to the “balling up” resulting from the formation of the liquid phase between Au and Ge, makes the accuracy of these resistivity values questionable, since the contact properties may vary appreciably over the whole contact area.

Alloyed Au–Ge–Ni contacts are also used to produce ohmic contacts to modulation-doped field-effect transistors [46–48]. To achieve this, the metallization should penetrate through the nearly non-conducting high band gap material to form extremely low resistance ohmic contacts with the low band gap material containing the two-dimensional electron gas (2DEG). This task must be carried out maintaining a surface morphology smooth enough to facilitate easy alignments, with no sideways spreading which could short out small geometry devices [46]. The real conduction mechanism from the alloyed region to the 2DEG in the unaffected region is not yet clear. Ketterson et al. [47] proposed that the current flows by tunneling from the contact region, where the metal and the semiconductor may be non-uniformly mixed in grains, laterally into the 2DEG.

Excellent reviews of the theory and fabrication technologies for ohmic contacts to III–V compound semiconductors can be found in refs. [49–52].

2.3. Vertical and horizontal current flow

Fig. 4 shows two metal films in contact with the opposite sides of a homogeneous semiconductor bar. For metal films sufficiently thick to be considered equipotential, the application of a voltage between A and B would force the flow of a current distributed uniformly through the contact interface. In principle, the contact resistance R_c corresponding to each interface can be determined by subtracting the resistive contribution of the semiconductor from the total resistance measured between A and B:

$$R_c = \frac{1}{2}(R_{\text{tot}} - \rho_b L/S), \quad (2.4)$$

where L and S are the length and the cross-sectional area of the bar, ρ_b the corresponding electrical resistivity, and the two contact interfaces have been assumed identical. Then, from eq. (2.4) the contact resistivity ρ_c could be obtained as

$$\rho_c = R_c S, \quad (2.5)$$

which is the typical relation valid for a vertical-type contact, namely a contact crossed by a uniform current distribution. Of course this is not a practical procedure to analyze a low-resistance contact interface, since in this case the corresponding resistive contribution would be an extremely small fraction of the measured total resistance. Moreover, this structure is not compatible with the monolithic integrated circuit technology.

Fig. 5 shows a second type of contact [53,54] which is of great importance in the planar semiconductor technology. The structure can be subdivided into the following main parts: (a) the metal film; (b) the semiconductor layer outside the contact, of sheet resistance R_{sh} ; (c) the semiconductor layer underneath the contact, of sheet resistance R_{sk} ; (d) the ohmic interface layer.

As we will see in detail below, the distinction between the semiconductor layers outside and underneath the contact is often required for an accurate determination of the contact resistivity, since metallurgical reactions occurring in the contact preparation process may lead to appreciable modifications in the value of the sheet resistance underneath the contact [55].

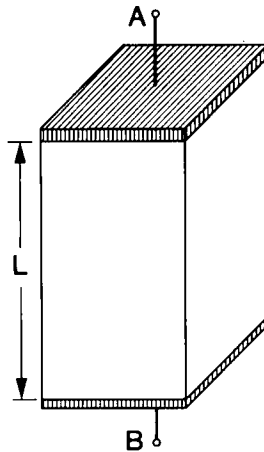


Fig. 4. Schematic diagram of two vertical-type contacts on the opposite sides of a homogeneous semiconductor bar. The current flow is uniformly distributed through the contact interface.

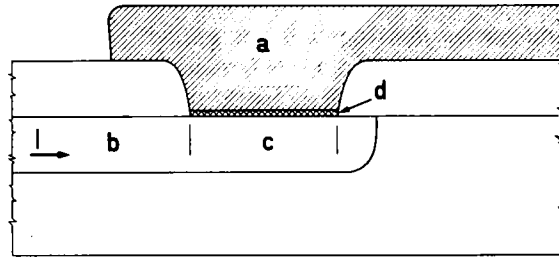


Fig. 5. Cross section of a horizontal-type contact: (a) metal film; (b) semiconductor outside the contact; (c) semiconductor under the contact; (d) interface layer.

All the models describing this type of contact are based on two fundamental assumptions:

(a) The interface region is uniform, which means that the mathematical models cannot be applied when precipitates or etch pits are present at the contact interface.

(b) The semiconductor layer underneath the contact as well as the metal film have thickness zero; in particular the junction depth Z_j is assumed to be equal to zero.

Under these hypotheses, the current flow is horizontal in both the semiconductor layer and the metal, while it is vertical at the interface. This is in fact referred to as the horizontal-type contact. The characteristics of the current flow lead to current crowding at the contact edge. As a consequence, in this case the contact resistivity characterizing the interface cannot be derived by eq. (2.5) from the resistive drop associated with the contact interface, because of the non-uniform current distribution across the contact.

From a practical point of view, the characterization of a horizontal contact is performed in two steps. The first step consists of the measurement of the contact resistance associated with the particular contact interface, which is carried out by measuring the voltage drop across the contact, at a known current, in specially designed test patterns. For this purpose, table 1 reports the most typical techniques for the evaluation of ρ_c [53,56–60], whereas the corresponding test devices are shown in figs. 6–9. The contact resistance for each structure is simply given by this voltage drop divided by the source current. The second step is based on the accurate extraction of the contact resistivity from contact resistance data. This can only be achieved through the development of models that allow the accurate prediction of the electrical behaviour in the test structures used for the measurements. In section 2.4 we will present a theoretical formulation of the problem together with the typical approximations applied, in practice, to make equations and boundary conditions easier to manage from a mathematical point of view, although still producing useful insights.

2.4. Theoretical models

In principle, an arbitrary semiconductor structure can be accurately analyzed in three dimensions using a mathematical model based on the Poisson and the two-carrier continuity equations, having as dependent variables the potential $v(x, y, z)$, and n and p (the electron

Table 1

TLTR	transmission line tap resistor
CTLR	circular transmission line resistor
CKR	cross Kelvin resistor
CER	contact end resistor

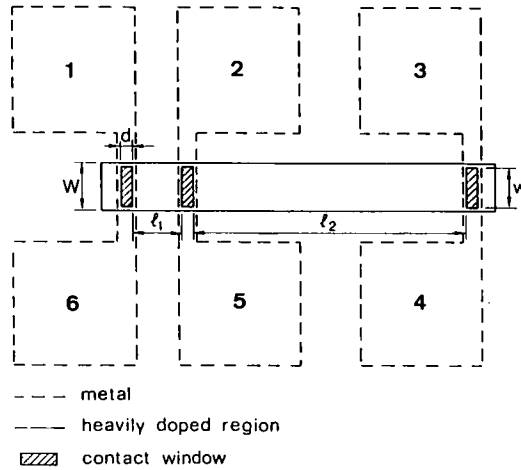


Fig. 6. The transmission line tap resistor (TLTR).

and hole concentration, respectively). In many cases, however, and the contact system is one of these, the device under consideration is intrinsically two (or even one) dimensional. Therefore, one can assume that the partial derivatives, in the basic equations, perpendicular to a given plane (or line) vanish, drastically simplifying the analytical or numerical solution of the problem.

As far as the contact system is concerned, the rigorous description in three dimensions of a generic structure with no restriction in the topology has been presented by Loh et al. in refs. [32,61,62] and subsequently extended by Scorzoni and Finetti [63]. The mathematical formula-

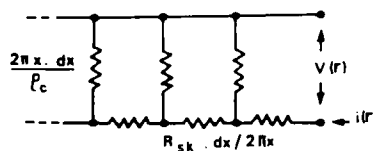
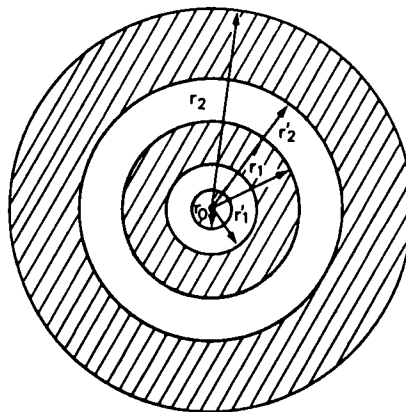


Fig. 7. The circular transmission line resistor (CTLR) and the transmission line model parameters.

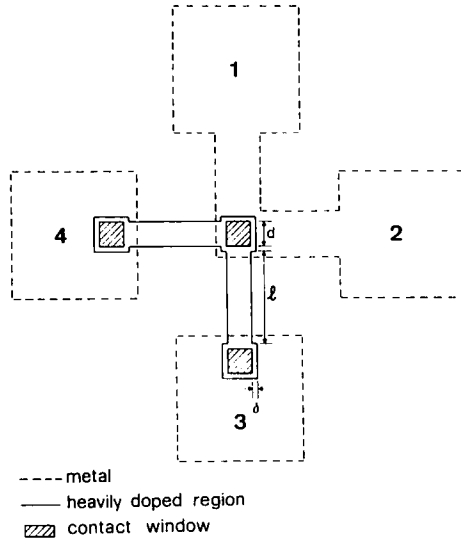


Fig. 8. The D-type cross Kelvin resistor (CKR).

tion was derived under the basic assumptions of negligible minority carrier effects and majority carrier concentration equal to the electrically active dopant density. Because of the difficulties in the computational work, it is advantageous to reduce the equations and boundary conditions to a two-dimensional form, which still gives consistent results.

Following ref. [32], let us consider the contact structure as a two-dimensional (2-D) surface perpendicular to the z axis (fig. 10). In this formulation, all the effects of the z axis, related to

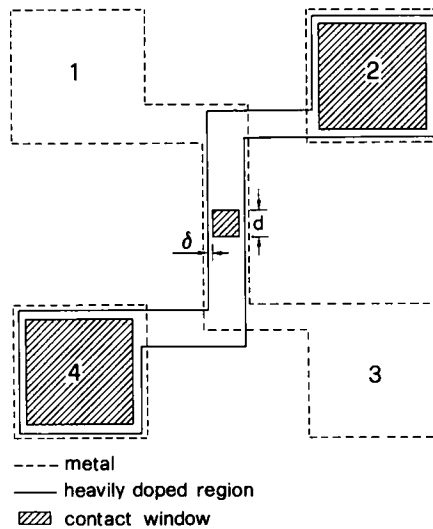


Fig. 9. The contact end resistor (CER).

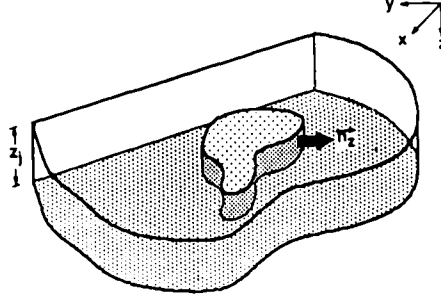


Fig. 10. General topology of the contact system. The contact surface is located at $Z = 0$; Z_j is the effective thickness of the semiconductor layer. From ref. [32]. © 198-IEEE.

the finite junction depth underneath the contact, Z_j , are lumped into one single parameter, that is the sheet resistance defined as

$$R_{sh} = \left(\int_0^{Z_j} \sigma(z) dz \right)^{-1}, \quad (2.6)$$

where the conductivity σ is assumed to be independent of x and y , as expected for planar diffused layers. It must be remarked that for special structures requiring deep junctions the effect of the z axis might be important. This has been studied by Schuldt [64] and Woelk et al. [65].

A new potential $V(x, y)$ has then to be introduced by defining the conductivity-weighted average of the potential $v(x, y, z)$ in the diffusion layer as

$$V(x, y) = \left(\int_0^{Z_j} \sigma(z) v(x, y, z) dz \right) \left(\int_0^{Z_j} \sigma(z) dz \right)^{-1} = \langle v \rangle_\sigma. \quad (2.7)$$

Since the metal layer is usually much more conductive than the semiconductor layer, the metal potential can be considered constant (typically at zero) over the entire interface. The contact system can be therefore completely characterized by the potential $V(x, y)$. Because of the possible differences in sheet resistance outside and underneath the contact, two conductivity-weighted average potentials, V_{out} and V_{in} (outside and underneath the contact respectively) should be introduced in the calculations. In the system described above, the majority carrier continuity equation in the diffusion area outside the contact becomes

$$\nabla \cdot \mathbf{J} = \partial J_x / \partial x + \partial J_y / \partial y = 0 \quad (2.8)$$

and the current density in the semiconductor is given by

$$\mathbf{J} = -\sigma \nabla_t V_{out}, \quad (2.9)$$

where ∇_t is a convenient 2-D gradient operator defined as

$$\nabla_t = \mathbf{a}_x \partial / \partial x + \mathbf{a}_y \partial / \partial y \quad (2.10)$$

and \mathbf{a}_x , \mathbf{a}_y are the unit vectors. By defining ∇_t^2 as the associated Laplacian, eq. (2.8) can be written as

$$\partial^2 V_{\text{out}} / \partial x^2 + \partial^2 V_{\text{out}} / \partial y^2 = \nabla_t^2 V_{\text{out}} = 0, \quad (2.11)$$

known as the Laplace equation. By conservation of the current, the following equation is shown to hold for the potential $V_{\text{in}}(x, y)$ at the contact interface

$$\nabla_t^2 V_{\text{in}} = V_{\text{in}} / l_t^2, \quad (2.12)$$

which is known as the Helmholtz equation. In eq. (2.12) the transfer length l_t is defined as $l_t = (\rho_c / R_{\text{sk}})^{1/2}$ where R_{sk} is the sheet resistance underneath the contact. As we shall see below, l_t indicates how far the current travels underneath the contact before being collected in the metal layer.

Furthermore the following matching conditions will hold at the contact periphery:

$$V_{\text{in}} = V_{\text{out}}, \quad (2.13a)$$

$$(\mathbf{n}_z \cdot \nabla_t V_{\text{out}}) / R_{\text{sh}} = (\mathbf{n}_z \cdot \nabla_t V_{\text{in}}) / R_{\text{sk}}, \quad (2.13b)$$

where \mathbf{n}_z is the unit vector orthogonal to the contact boundary and perpendicular to the z axis. Defining

$$\Omega = R_{\text{sk}} / R_{\text{sh}}, \quad (2.14)$$

eq. (2.13b) may be written as

$$\Omega (\mathbf{n}_z \cdot \nabla_t V_{\text{out}}) = \mathbf{n}_z \cdot \nabla_t V_{\text{in}}. \quad (2.15)$$

Once the voltage distribution is known, the total current flowing in the contact system can be calculated as

$$I_{\text{tot}} = - \frac{1}{R_{\text{sh}}} \int \nabla_t V_{\text{out}} \cdot d\mathbf{l}_n, \quad (2.16)$$

where \mathbf{l}_n is any line of the x - y plane crossed by I_{tot} .

2.5. Scaling theory and generalized simulation curves

As we have seen in the previous paragraph, given a transfer length l_t and a particular contact geometry, by solving the Laplace and Helmholtz equations one can determine the potential distribution throughout the diffusion layer. In order to determine the contact resistance, the corresponding voltage drop is detected at a position dependent on the particular test device (see for example figs. 6–9). If V^* is the generic measured voltage, the ratio between V^* and the total current crossing the contact can be expressed as a function of l_t as

$$\frac{R^*(l_t)}{R_{\text{sh}}} = - V^* \left(\int \nabla_t V_{\text{out}} \cdot d\mathbf{l}_n \right)^{-1}. \quad (2.17)$$

This means that in two-dimensional simulations of a specified test structure geometry, l_t can be used as a single independent parameter.

At this point it can be observed that, if the structural dimensions and the transfer length are scaled by an arbitrary length L , the equations governing the electrical behaviour of the contact structure become the following

$$\frac{\partial^2 V_{in}}{\partial (x/L)^2} + \frac{\partial^2 V_{in}}{\partial (y/L)^2} = \frac{V_{in}}{(l_t/L)^2}, \quad (2.18a)$$

$$\frac{\partial^2 V_{out}}{\partial (x/L)^2} + \frac{\partial^2 V_{out}}{\partial (y/L)^2} = 0. \quad (2.18b)$$

Since they maintain the same form as before scaling, the potential distribution corresponding to the scaled structure will be the same as for the original one. Furthermore, it can be easily seen that the total current flowing in the contact structure will not be modified after scaling. As a consequence, the ratio R^*/R_{sh} will retain the same form as in eq. (2.17), but the independent parameter will now be l_t/L . Moreover, by introducing in the logical deduction the matching conditions (2.13a) and (2.15), the resistance R^* of the structure, normalized to R_{sh} , can be written as [63]

$$\frac{R^*}{R_{sh}} = \frac{R^*}{R_{sh}} \left(\frac{\text{dimensions}}{L}, \frac{l_t}{L}, \Omega \right). \quad (2.19)$$

Numerical simulations of the ratio R^*/R_{sh} can be normalized, providing for each particular test structure (TLTR, CKR or CER) a set of generalized curves based on non-dimensional parameters. In particular in the following we will assume for convenience $L \equiv \delta$, where δ is the alignment tolerance defined in figs. 6–9. The use of the scaling law shown in eq. (2.19) allows drastic simplification of the simulation work required for the extraction of the contact resistivity from contact resistance measurements in the different test patterns.

2.6. Test structures for the extraction of the contact resistivity from contact resistance measurements

One method of classifying experimental values of contact resistivity is by the type of metallization. Table 2 shows, as an example, data relative to different types of silicides, reported in the literature by different authors [23–40]. A large spread in ρ_c can be observed. Although small differences in the surface dopant concentration can affect appreciably the resulting values of ρ_c , this can only partly explain the observed scattering, even for the same type of silicide. Quite generally, the contact resistivity depends on both the intrinsic characteristics of the silicide under test (such as the barrier height ϕ_B , or the capability of snow-plowing the dopant [41–45]) and the particularities of the contact preparation (from silicon surface cleaning to metal deposition and annealing conditions). Most often, however, the scattering arises from the individual test procedures used to evaluate ρ_c , since the accuracy of the different methods can differ appreciably. The CKR and CER, for example, allow the extraction of the contact resistivity from a single electrical measurement. On the contrary, in the case of the TLTR and CTLR the derivation of ρ_c is performed by means of several electrical measurements on contacts that are assumed of identical geometrical as well as physical characteristics.

Table 2

	ρ_c (Ω cm ²)	N (cm ⁻³)	Ref.
Pd ₂ Si	(6.3–23) $\times 10^{-7}$	n ⁺ (P) (3–5) $\times 10^{19}$	
	6.8×10^{-7}	p ⁺ (B) 1.0×10^{20}	[23]
Al/Pd ₂ Si	2.0×10^{-6}	n ⁺ (As)	[24]
Al/W/Pd ₂ Si	1.2×10^{-6}	n ⁺ (As)	[25]
Pd/Pd ₂ Si	$\sim 2 \times 10^{-6}$	n ⁺ (As) 2.0×10^{20}	[26]
Al/Pd ₂ Si–Ag/Pd ₂ Si	$\leq 4 \times 10^{-6}$	n ⁺ (P) 2.0×10^{20}	[27]
Al/Pd ₂ Si	7.0×10^{-8}	n ⁺ (P) 4.0×10^{20}	
	3.0×10^{-6}	p ⁺ (B) 1.0×10^{19}	[28,29]
Al/W/PtSi–Al/PtSi	(1–4) $\times 10^{-8}$	p ⁺ (B) 1.2×10^{20}	[30]
Al/W/PtSi/n ⁺ -polySi	4.5×10^{-8}	n ⁺ (P)	[31]
Al/W/PtSi	7.4×10^{-7}	p ⁺ (B)	[25]
Al/W/PtSi	5.1×10^{-8}	n ⁺ (P) $R_{sh} = 12.1$	[32]
Al/TiW/PtSi	$\sim 1 \times 10^{-6}$	n ⁺ (As) 1.7×10^{20}	[33]
Al/PtSi	4.4×10^{-7}	n ⁺ (As) 2.1×10^{20}	
	2.2×10^{-7}	3.0×10^{20}	
	7.8×10^{-8} a)	2.1×10^{20}	
	3.7×10^{-8} a)	3.0×10^{20}	
	4.3×10^{-7}	p ⁺ (B) 3.2×10^{19}	
	2.3×10^{-7} a)	3.2×10^{19}	[34]
Ag/Cr/PtSi	(4–8) $\times 10^{-6}$	n ⁺ (As) 1.1×10^{21}	
	$\geq 5 \times 10^{-5}$	p ⁺ (B) 2.4×10^{19}	[35]
PtSi	2.0×10^{-7} b)	n ⁺ (As) 4.2×10^{20}	[36]
TiSi ₂	8.5×10^{-9}	n ⁺ 9×10^{19}	[37]
Al/TiN/TiSi ₂	2.0×10^{-6}	n ⁺ (As) 1.7×10^{20}	[33]
Al/TiW/TiSi ₂	4.0×10^{-8}	n ⁺ (As) 6.6×10^{20}	
	1.5×10^{-7}	3.0×10^{20}	
	3.0×10^{-7}	1.5×10^{20}	
	7.0×10^{-7}	4.5×10^{19}	
	9.0×10^{-7}	2.5×10^{19}	[38]
Al/TiSi ₂	8.0×10^{-8}	n ⁺ (P) 2.0×10^{20}	
	6.0×10^{-5}	p ⁺ (B) 1.0×10^{19}	[28,29]
Al/TiSi ₂	1.0×10^{-7}	n ⁺ (As) 1.5×10^{20}	
	3.0×10^{-7}	p ⁺ (B) 6.0×10^{19}	[39]
NiSi	2.0×10^{-6}	n ⁺ (P) 2.0×10^{20}	[40]
Al/NiSi	5.0×10^{-8}	n ⁺ (P) 2.0×10^{20}	
	2.0×10^{-5}	p ⁺ (B) 1.0×10^{19}	[28,29]
Al/CoSi ₂	4.0×10^{-7}	n ⁺ (P) 2.0×10^{20}	
	4.5×10^{-7}	n ⁺ (As) 2.0×10^{20}	[29]
Al/CoSi ₂	1.0×10^{-7}	n ⁺ (As) 1.5×10^{20}	
	1.5×10^{-7}	p ⁺ (B) 6.0×10^{19}	[39]
Al/MoSi ₂	7.0×10^{-8}	n ⁺ (As) 2×10^{20}	[29]

a) Sputter etching prior to the Pt deposition and in situ heating were performed.

b) Depending on the preparation conditions.

It is worthwhile to stress that contact resistivity values in the low 10^{-8} Ω cm² range (and, a fortiori, in the 10^{-9} range) are very difficult to understand, also assuming that one can really measure them. In fact, WKB theoretical calculations by Boudville and McGill [4] indicate 10^{-8} Ω cm² as the lower limit attainable for contact resistivity, even at very high doping levels.

As we shall see, the 1-D equations commonly used to relate the contact resistance data to ρ_c in the different test structures are derived from distributed resistor networks. The fundamental assumption of the models simulating the TLTR, CTLR, CKR and CER behaviour is that the diffusion width is equal to the contact width. However, several problems arise in the extraction of ρ_c using this assumption, because of the presence, in actual structures, of a parasitic area around the contact, due to the alignment tolerance between diffusion and contact edges required in the lithographic process. Because of the consequent effects on the current distribution, as will be reported in the following, the CER and the CKR deviate appreciably (and in some cases dramatically!) from their 1-D predictions. It will be shown that in the case of the TLTR the deviation is less severe, whereas it could be completely avoided by using the corresponding circular transmission line resistor. However, in both cases, further problems arise, due to the indirect measurement of the desired voltage in this type of resistors.

In the following sections, the different methods for the determination of ρ_c will be described in detail. In particular the accuracy of the various measurement techniques and simulation models will be discussed for different values of contact resistivity, diffusion sheet resistance and contact geometry, in the case of contact metallizations of particular interest for applications in integrated circuit technology. Procedures aimed to make the extraction of ρ_c easier will be described. Recently developed test structures will also be presented.

3. Transmission line resistors

3.1. The transmission line tap resistor (TLTR)

Before describing this type of resistor (reported in fig. 6), it is necessary to give details on the transmission line model (TLM) introduced by Shockley [66] and subsequently refined by Berger [53,54] and by Murrmann and Widmann [67,68]. Let us first assume that the contact, rectangular in shape, is as wide as the diffused resistor, although this condition is ideal, due to the alignment tolerance requirements. This allows us to neglect potential variations in the y direction, and the problem can be treated as one-dimensional.

In this case, the Helmholtz equation previously presented in two dimensions becomes

$$\partial^2 V_{in} / \partial x^2 = V_{in}(x) / l_t^2, \quad (3.1)$$

which is the same equation describing the potential of a transmission line. In the papers cited above in fact the authors arrived at eq. (3.1) by modelling the contact system with a transmission line as shown in fig. 11, with the generic boundary conditions

$$dV_{in}/dx|_{x=0} = -R_{sk} I_1 / w, \quad (3.2a)$$

$$dV_{in}/dx|_{x=d} = -R_{sk} I_2 / w, \quad (3.2b)$$

where w is the contact width and I_1 and I_2 are the currents entering and leaving the contact region, respectively. Of particular interest is the case where $I_2 = 0$. The “front” resistance R_f is defined as the ratio of the voltage drop V_f across the interfacial layer at the front edge of the contact, where the current density is higher, to the total current I_1 flowing through the contact. In particular, R_f is described by the following equation

$$R_f = V_f / I_1|_{I_2=0} = Z \coth(d/l_t), \quad (3.3)$$

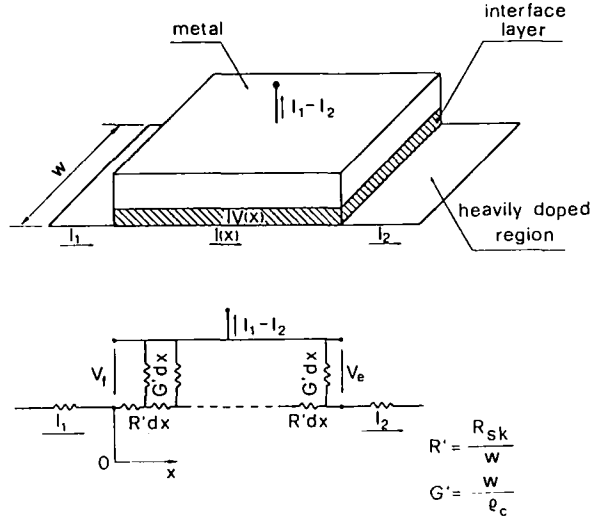


Fig. 11. Comparison of the contact region with a transmission line.

where d is the contact length and $Z = (R_{sk} \rho_c)^{1/2} / w$ and l_t are the characteristic impedance and transfer length of the line, respectively.

For the usual case $w < W$, where W is the diffusion width, eq. (3.3) only approximates the real contact resistance. In fact the non-uniform current distribution around the contact when $w < W$ is not taken into account by the conventional TLM.

For “electrically long” contacts (i.e. in the case of $d \ll l_t$) the contact resistance is given by the characteristic impedance of the line. Concerning the transmission length, its meaning is well clear if we consider the current distribution $I(x)$ underneath the contact for electrically long contacts. It can be written as

$$I(x) = I_1 \exp(-x/l_t). \quad (3.4)$$

At a distance l_t from the front edge of the contact, the current flowing in the semiconductor is reduced by a factor $1/e$, i.e. about 63% of the total current entered the metal. By decreasing l_t , at decreasing contact resistivity or increasing sheet resistance, the current crowding underneath the contact is accentuated. On the contrary, for increasing values of l_t , the structure approaches a vertical type contact, since the semiconductor layer tends to become equipotential. In fact, for l_t going to infinity R_t assumes the following expression

$$R_t \xrightarrow{l_t \rightarrow \infty} \rho_c / wd, \quad (3.5)$$

which is characteristic of a vertical contact of area wd . The same result can be obtained also when the condition $d \ll l_t$ is true.

The theory reported above can be applied to the so-called transmission line tap resistor. In its first version this was made of several planar contacts on an implanted or diffused semiconductor substrate, the various contacts being at a constant distance from each other. In a subsequent version the contacts were differently spaced. In this report we will examine in detail this second type of structure (shown in fig. 6), which has received considerable interest from both the theoretical and experimental point of view.

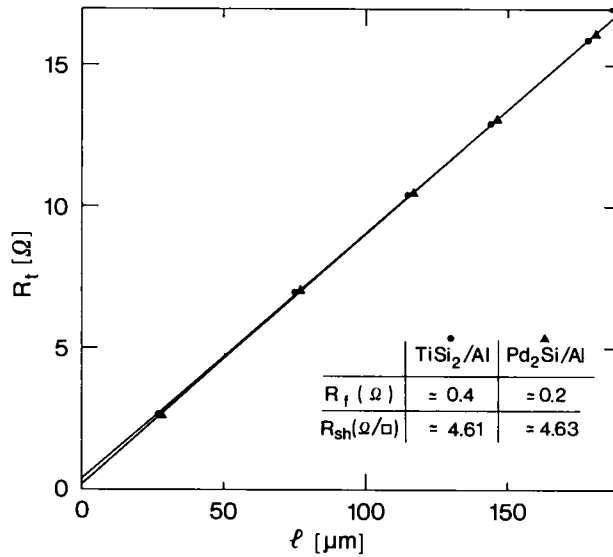


Fig. 12. Characteristic plot of the total resistance as a function of the contact separation in a TLTR structure. The nominal dimensions were $l_1 = 30$, $l_2 = 80$, $l_3 = 120$, $l_4 = 150$, $l_5 = 180$, $w = 40$, $W = 50 \mu\text{m}$.

For contacts of identical geometrical and electrical characteristics the following expression holds for each pair of contacts

$$R_{ti} = 2R_t + R_{sh}l_i/W, \quad (3.6)$$

where R_{ti} is the total resistance measured between the two contacts at a separation l_i . It can be observed that, to exclude any contact resistance introduced by the probes (see fig. 6), current (1 and 2) and voltage (6 and 5) probes are separated. By plotting R_{ti} as a function of l_i , one can derive a graph similar to the one shown in fig. 12, determined in the case of TiSi₂ and Pd₂Si contacts on n⁺-Si. In the figure, the solid lines are least-squares interpolations of the experimental data. The value of the front contact resistance is then obtained by the intercept of the line with the resistance axis, whereas the sheet resistance of the diffused layer is determined from the slope. The comparison of R_{sh} derived in this way with the values of R_{sh} obtained by four-point-probe measurements on plain diffused wafers is typically a confirmation of the consistency of the results.

When it is possible to assume that the sheet resistance underneath the contact is not modified in the contact preparation procedure (so that $R_{sk} = R_{sh} = R_s$) the contact resistivity can be determined by applying eq. (3.3). Although two independent measurements are sufficient to obtain the two unknown parameters of the problem, namely the contact resistivity and the sheet resistance, several contacts are typically used in order to improve the accuracy of the method.

It is well known that the alloying-sintering process occurring at the metal/semiconductor interface can lead to appreciable modifications of the sheet resistance underneath the contact, R_{sk} . In this case a further resistance measurement is required to determine ρ_c , R_{sk} and R_{sh} . The additional measurement has been suggested by Berger [54], then developed by Chang [69]

and Reeves and Harrison [70]. It consists of the measurement of the end resistance, defined by following the mathematical formulation of the transmission line (fig. 11), as

$$R_e = V_e/I_1 |_{I_2=0}. \quad (3.7)$$

The mathematical expression of the end resistance can be easily derived as

$$R_e = \frac{Z}{\sinh(d/l_t)} = \frac{\rho_c}{l_t w} \frac{1}{\sinh(d/l_t)}. \quad (3.8)$$

It can be observed, however, that R_e is quite a critical parameter. In fact, in the case of a small transmission length (for example for $\rho_c = 1 \times 10^{-7} \Omega \text{ cm}^2$ and $R_{sk} = 30 \Omega/\square$ then $l_t = 0.58 \mu\text{m}$) a contact length equal to $3l_t$ determines a value of R_e which is about 5% of the corresponding front resistance ($R_f = Z = 1.7 \Omega$ for $w = 10 \mu\text{m}$). As a consequence, the end resistance becomes vanishingly small as the contact length increases, thus making its accurate determination difficult, and in some cases even impossible. The optimization of the contact geometry to the measurement of R_e allows the determination of the parameter l_t by the implicit relation

$$R_f/R_e = \cosh(d/l_t), \quad (3.9)$$

or, by developing the previous expression,

$$l_t = \frac{d}{\ln\left\{R_f/R_e + \left[(R_f/R_e)^2 - 1\right]^{1/2}\right\}}. \quad (3.10)$$

Once l_t is known, ρ_c and R_{sk} can then be calculated from the equations

$$\rho_c = R_e l_t w \sinh(d/l_t), \quad (3.11a)$$

$$R_{sk} = \rho_c/l_t^2. \quad (3.11b)$$

Both types of measurements were carried out by Reeves and Harrison [70] in the characterization of alloyed Au-Ge-Ni contacts on n-type GaAs epitaxial layers and of sintered Al metallizations on Sb-ion-implanted Si. The data reported by these authors indicate the importance of including the modified sheet resistance in the calculations of the contact resistivity. However, it has to be noticed that the contact length used in these experiments was $50 \mu\text{m}$. This value is convenient for the analysis of contact structures with comparably high transfer length values, but absolutely critical when characterizing contacts with low contact resistivity and high sheet resistance.

3.2. Parasitic effects

The transmission line tap resistor has been largely used since the 70s to characterize the metallization systems of major interest in the semiconductor technology. In particular, the contact resistivity of pure Al and Al-Si alloys on silicon has been extensively monitored as a function of the deposition characteristics, dopant concentration and annealing procedures.

However, since the beginning of these studies, it was realized that parasitic effects, not taken into account in the transmission line theoretical model, could possibly affect the accurate extraction of ρ_c from front resistance data.

In fact the mathematical procedure presented so far is based on the assumption of identical contact and diffusion widths, w and W respectively. In practice, however, the contact width is smaller due to the alignment tolerance and lateral current crowding occurs in the diffusion area around the contact. The consequent effect on the extraction of the contact resistivity from contact resistance data has been analyzed independently by Ting and Chen [71], by Chang [69] and by Berger [54] at the beginning of the 70s, and recently by Loh et al. [32,62].

In ref. [54] the lateral current crowding effect has been decomposed into two different contributions, mutually interacting and having opposite consequences on the measurement of R_f .

The first one, referred to as the lateral effect, is caused by current flowing laterally in the diffusion region outside the contact, which gives an additional contribution to the measured total resistance.

Since the contact sides are partly used for the current flow, a second contribution referred to as the gap effect occurs, which reduces the overall contact resistance.

The first contribution has been calculated by Ting and Chen by conformal mapping and the following expression has been derived in the case $\delta = (W - w)/2 \ll W$ [71]

$$R_w = \frac{R_{sh}}{2\pi} \left(\frac{1}{k} \ln \frac{k+1}{k-1} + \ln \frac{k^2-1}{k^2} \right), \quad (3.12)$$

where

$$k = \frac{W}{W-w} = \frac{1}{2} \frac{w}{\delta} + 1. \quad (3.13)$$

In the case of high values of δ , the corresponding overestimation of R_f , due to this effect alone, could be quite appreciable, as the experimental data presented by Naguib and Hobbs [72] seem to indicate.

In ref. [69], Chang considered the gap effect alone, by shunting the diffusion layer sheet resistance of the TLM by the resistances contributed by the two gaps between the contact and diffusion layer edges. The values of contact front resistance calculated from the expression

$$R_f = \left\{ \left[\left(\frac{R_{sk}}{W-2\delta} \parallel \frac{R_{sh}}{2\delta} \right) \frac{\rho_c}{W-2\delta} \right]^{1/2} \left\{ \tanh \left(\left[\left(\frac{R_{sk}}{W-2\delta} \parallel \frac{R_{sh}}{2\delta} \right) \frac{W-2\delta}{\rho_c} \right]^{1/2} d \right) \right\}^{-1} \right\}, \quad (3.14)$$

where the symbol \parallel stands for the parallelism of the resistances, fit satisfactorily the experimental data reported in his work.

Fig. 13 shows the comparison between the front resistance as calculated from the TLM 1-D model, and the values as predicted by using a pseudo-three-dimensional resistor network for square contacts of size $d = w$ in the case $\Omega = 1$. Fig. 13 shows the values of R_f/R_{sh} versus d/δ , with l_1/δ considered as a parameter. In fact, referring to eq. (2.19), it is possible to write

$$\frac{R_f}{R_{sh}} = \frac{R_f}{R_{sh}} \left(\frac{d}{\delta}, \frac{l_1}{\delta} \right). \quad (3.15)$$

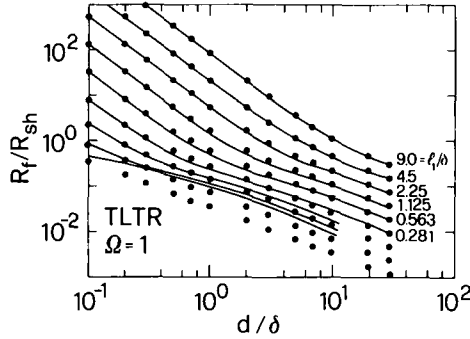


Fig. 13. Generalized extraction curves (solid lines) for a square-contact TLTR. The parameter l_1/δ is in octave steps and $\Omega = 1$. For comparison, 1-D calculations are reported as dots.

The simulation model, which is described in detail in refs. [73,74], is derived by a finite-differences discretization. As shown in fig. 14 the active region of the contact is divided into cubic cells, and R_x , R_y and R_z are related to the sheet resistance of the diffused layer underneath and outside the contact region, and to the contact resistivity, respectively. The exponential decay of the current in the semiconductor–contact system near the edge of the contact has been taken into account by properly subdividing that region in a very fine mesh with resolution equal to $l_1/3$. Furthermore, the metal layer has been assumed equipotential. By solving numerically the standard circuit laws, for given contact geometry, R_{sh} , R_{sk} and ρ_c , then the voltage distribution in the contact and diffusion regions, at a particular current value, can be determined. By subtracting the series resistance of the diffusion layer from the total resistance between the input and output current terminals one can immediately determine the

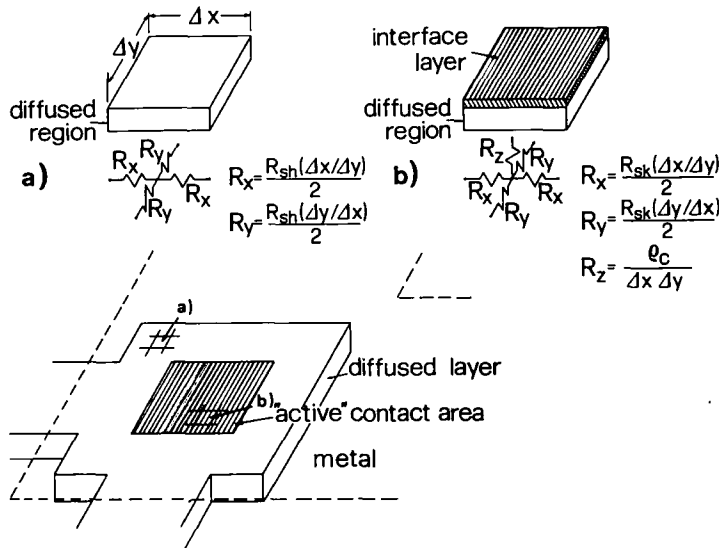


Fig. 14. Schematic of the planar ohmic contact and description of the elementary cells outside (a) and inside (b) the “active” contact area.

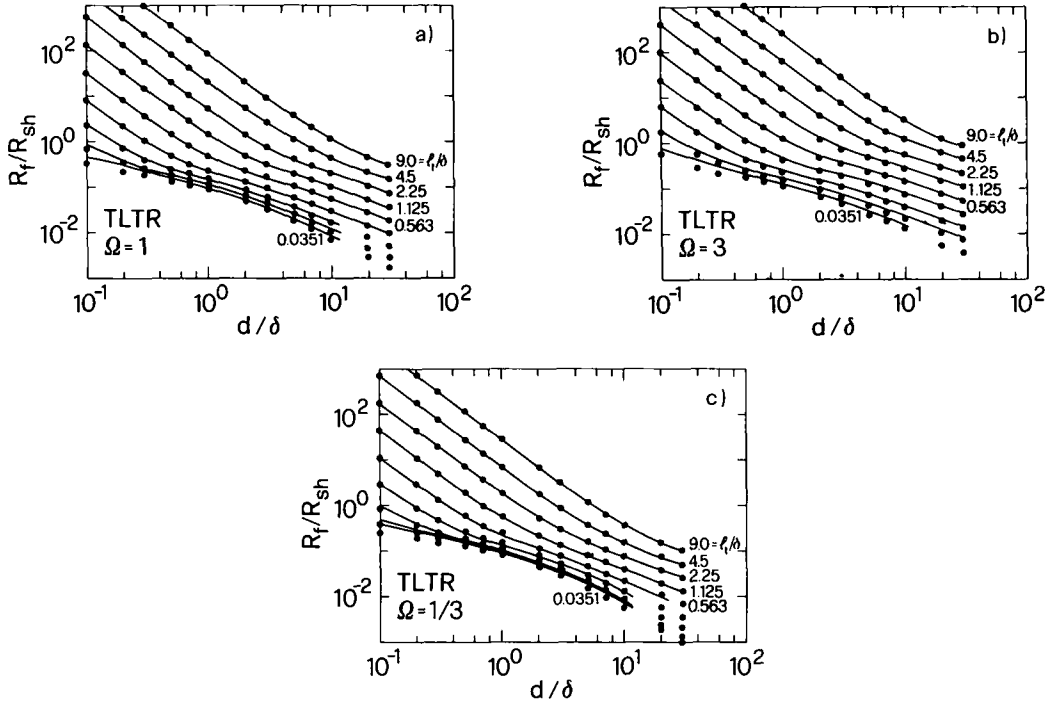


Fig. 15. Generalized extraction curves (solid lines) for a square-contact TLTR in the cases $\Omega = 1$ (a), 3 (b) and $1/3$ (c). The parameter l_i/δ is in octave steps. For comparison, analytical calculations from refs. [69,71] are reported as dots.

front resistance associated with the particular contact geometry. This has been done by drawing a set of generalized curves corresponding to all practical values of contact resistivity, sheet resistance and dimensions.

In general, one can observe that for $\rho_c > 1 \times 10^{-7} \Omega \text{ cm}^2$ and $W - w$ on the order of $0.1W$ the predictions of the 1-D model are in quite good an agreement with the results predicted by the computer simulations. As a consequence, in most of the work reporting experimental data of contact resistivity using the transmission line tap resistor the results were not appreciably affected by parasitic effects.

However, in fig. 13 we can observe an appreciable disagreement between the two models in the intermediate d/δ range and for extremely low $l_i/\delta (< 0.2)$, i.e. for values typical of VLSI structures. In this case the parasitic effects should be taken into account by proper simulations. For this purpose we have compared the predictions resulting from the analytical expressions (3.12)–(3.14) to the numerical 2-D simulations. The results are shown in figs. 15a, 15b and 15c, for square contacts and $\Omega = 1$, 3 and $1/3$ respectively. Eqs. (3.12) and (3.14) have been rewritten as functions of non-dimensional parameters and the corresponding R/R_{sh} values have been added in order to include both the contributions. In all cases very good agreement between numerical and analytical data was achieved, confirming the validity of the simple analytical models. Only below an extremely low threshold of l_i/δ (equal to 0.1) can a slight discrepancy be observed. Further explanations on the use of the generalized extraction curves can be found in the next sections.

3.3. Electrical characterization of conventional metal systems on silicon

Improvements in the contact resistance performance represent an important task in integrated circuit technology. In order to monitor accurately this parameter, the transmission line tap resistor has been extensively applied in the past. Contact resistivity values of several metal systems have in fact been reported for different semiconductor substrates, doping concentrations and annealing procedures.

As far as Al-based metallizations on heavily doped Si are concerned, an extensive characterization of Al-Si contacts has been carried out by Berger [54] on n- and p-type silicon at different doping levels. In particular, upon sintering at 400 °C for 20 min, good ohmic contacts could be achieved on n-Si, for surface concentrations above $5 \times 10^{19} \text{ cm}^{-3}$. At the highest doping levels, ρ_c values in the range $(0.5-1) \times 10^{-6} \Omega \text{ cm}^2$ were determined.

In ref. [72], Naguib and Hobbs applied the transmission line tap resistor to determine the effect of sintering and doping level on the front resistance of Al/Si and Al/poly-Si contacts. In both cases sintering at 450 °C showed the lowest contact resistance. However, the authors did not try to extract contact resistivity values from the measured resistance data.

In ref. [75], Finetti et al. investigated the contact characteristics of different Al-based contact structures (Al, Al-Si, Al/undoped polySi, Al/n⁺-polySi) on n⁺-Si. In this case, the transmission line tap resistor consisted of a self-aligned structure obtained by a two-mask process, where current crowding effects could be avoided, except for the negligible effect related to the lateral dopant diffusion. Measurements were carried out as a function of the post-metallization annealing temperature (see fig. 16). For comparison, a Ti/Ag metallization was also characterized. Minimum values of ρ_c in the range of $(1-2) \times 10^{-6} \Omega \text{ cm}^2$ were measured in the case of pure Al deposited directly on n⁺-Si, after a thermal treatment at 450 °C for 30 min. The effect of multi-scan electron beam sintering on the contact resistivity of Al-Si contacts on n⁺-Si was studied in ref. [76], in order to avoid the formation of Al spikes short circuiting the underlying junction. The same authors improved the TLM considering the possibility of a finite resistivity of the metal layer. Other approaches to the problem of the non-zero metal sheet

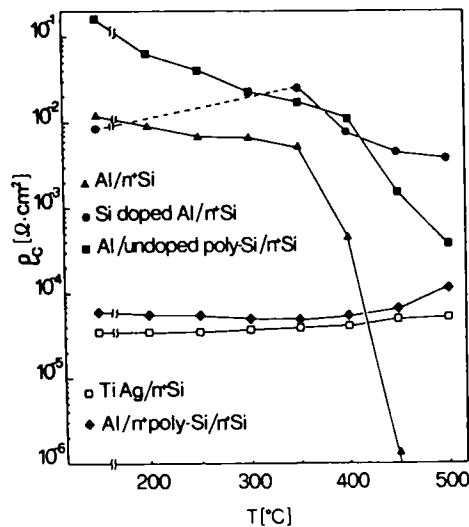


Fig. 16. Contact resistivity versus post-metallization annealing temperature for different metal/semiconductor structures.

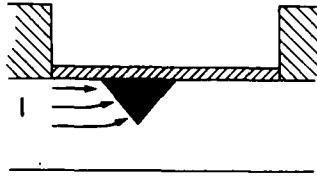


Fig. 17. The effect of heavy pitting on the contact current distribution.

resistance can be found in refs. [77–79] and in ref. [80], where Scott et al. developed a transmission line model taking into account silicide diffusions.

In ref. [81] results were reported on the contact resistance of Al–Si ohmic contacts on p^+ -Si layers, sintered by rapid lamp annealing. A marked improvement in the contact resistance as well as in the contact uniformity was observed with respect to conventional furnace sintering at 430°C for 15 min. In particular, a specific contact resistance equal to $4 \times 10^{-6} \Omega \text{ cm}^2$ was measured by applying the TLTR, for an estimated boron surface concentration of $1 \times 10^{19} \text{ cm}^{-3}$, and following a 20 s sintering at 450°C .

It is however to be observed that the uniformity of the contact interface is a fundamental assumption on which the transmission line tap resistor, as well as all the resistor structures that will be described in the following, are based. As a consequence, the contact resistivity data extracted for the pure Al metallization refer to the hypothetical case of the absence of pits at the contact interface. Because of the well-known Al/Si interface pitting, modifications in the measured resistance are expected. Due to the pitting, in fact, the effective contact area is increased but, above all, the interface planarity is destroyed with consequent heavy modification of the current distribution within the contact region, due to a mixture of vertical–horizontal current flow (see fig. 17). This effect is neglected by all the simulation procedures based on the hypothesis of horizontal-like contact structures. As a consequence, the values of contact resistivity derived for this metallization have to be considered as semi-quantitative estimates of the contact resistivity, since they can be strongly affected by the particular interface morphology.

The same considerations obviously apply to the general case of contact inhomogeneities, due to a rough and laterally non-uniform interface (i.e. Au–Ge–Ni on GaAs alloyed ohmic contacts) or to particle precipitation (i.e. Al–Si alloys on Si). Concerning this difficulty, an example of application of the TLTR to planar metal/GaAs interfaces is represented by the Ge/ n^+ -GaAs heterostructure. In ref. [82], Marshall et al. studied the solid-phase epitaxial growth (SPEG) of Ge on GaAs, using Pd as a transport medium. Contact resistivity values for Ge/Pd/GaAs and Ge/Pd(Sb)/GaAs, where Sb was incorporated to interstitially doped Ge during contact sintering are shown in fig. 18, where the lower curve refers to the sample incorporating the Sb thin film. The trend in the experimental data was of practical help to better understand the mechanism of ohmic contact formation, and in particular to the dependence of Ge transport on annealing temperature and time, as well as the beneficial effect of incorporating a dopant species in the metallization structure.

Due to the continuous scaling down of integrated circuit device dimensions, the formation of low-resistance and reliable ohmic contacts on shallow junctions has become of primary importance. In particular, ρ_c values below $1 \times 10^{-6} \Omega \text{ cm}^2$, as typically measured in Al-based metallizations, are required. For this purpose, new materials and new deposition techniques have been developed recently. Metal silicides and CVD tungsten films offer effective solutions for submicron VLSI metallization problems. Thin films acting as diffusion barriers between a silicide and an Al overlayer have also been studied with large interest, for applications in VLSI.

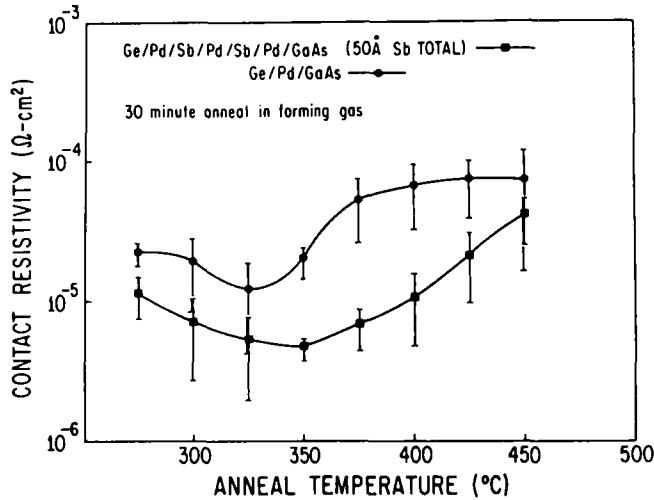


Fig. 18. Contact resistivity as a function of annealing temperature after a 30 min anneal for Ge/Pd/GaAs and Ge/Pd(2×25 Å Sb)/GaAs samples. The points represent the average measured values and the bars represent the spread in measured values. From ref. [82].

As a consequence of this trend several papers have been presented recently in the literature, reporting on the contact resistivity of advanced metallization systems on Si-doped layers [21,28,30,33,62,83].

The effect of the presence of silicide sidewalls at the entrance of the contact (fig. 19) on the measured contact resistivity has been examined quantitatively in ref. [28]. A mixture of horizontal and vertical current flows is introduced, depending on the silicon thickness consumed during the silicide formation. It was shown that the error on ρ_c is appreciable only for low contact resistivity values. For example, in the case of $\rho_c = 10^{-7} \Omega \text{ cm}^2$ the error is negligible for $R_{sk} = 5 \Omega/\square$, whereas errors up to 40% are expected for $R_{sk} = 100 \Omega/\square$.

The transmission line tap resistor has been extensively used by Nicolet's group at Caltech to characterize the electrical properties of diffusion barriers deposited directly on heavily doped silicon or incorporated between a silicide and a thick aluminum overlayer. In particular results have been reported on the contact resistivity of reactively sputtered TiN on n^+ - and p^+ -Si [21], and in the case of sputtered metallic amorphous alloys such as FeW [83]. The contact resistivity of NiSi films and the effect of ion implantation on the electrical properties of the corresponding interfaces have also been analyzed.

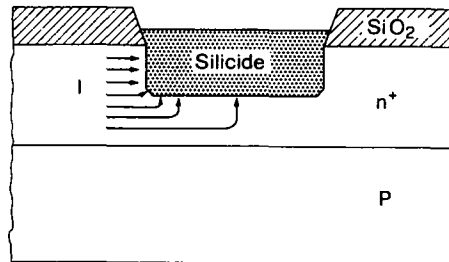


Fig. 19. Illustration of the mixture of horizontal and vertical current flows caused by the presence of silicide side-walls at the contact. From ref. [28].

In ref. [33], Ting and Wittmer reported on the contact resistivity of different metallization systems based on the Ti technology and characterized by applying the transmission line tap resistor on As-doped silicon.

Swirhun et al. [30] characterized the contact resistivity of Al/W/ n^+ -Si and Al/W/ p^+ -Si for a range of surface concentrations likely to be encountered in devices, as well as the contact resistivity for the Al/W/PtSi/ p^+ -Si contact system. Values as low as $4 \times 10^{-8} \Omega \text{ cm}^2$ (on $1.2 \times 10^{20} \text{ B/cm}^3$) have been determined for the Al/W/PtSi structure, although the measurement of so low values by using this technique requires extremely accurate electrical and optical measurements of the test device. Similarly values of contact resistivity on the order of 10^{-7} – $10^{-6} \Omega \text{ cm}^2$, depending on surface doping concentration, have been found for the Al/W/ n^+ -Si and p^+ -Si structures.

Since the consistency of the values of ρ_c extracted from front resistance data on differently shaped test structures is an indication of the validity of the experimental procedure, fabrication of test structures with different geometries is highly desirable. In ref. [62] this has been carried out, together with an extensive use of the previously described generalized extraction curves. In this case the Laplace and Helmholtz equations were numerically solved in the contact region and in the remainder of the diffusion region respectively, using a modified version of PISCES [61]. ρ_c values on the order of $(1.8\text{--}2.6) \times 10^{-7} \Omega \text{ cm}^2$ were successfully extracted from square-contact TLTR structures with varying d and δ . For an accurate procedure, the separation distances and the overlaps in the measured test structures were carefully determined by optical and electrical techniques. The values of l_i/δ corresponding to each experimental point have been derived from the R_i/R_{sh} and l/δ values, and multiplied by the measured value of δ . Then, by knowing R_{sh} the relative value of contact resistivity could be determined. The accuracy of the procedure is indicated by the fact that all the extracted ρ_c values are within 20% of each other. Unfortunately, the authors did not specify the type of metallization they were characterizing. Although this represents a neat piece of work, it should be observed that the range of l_i/δ where the method is applied is sufficiently high that the classical TLM could give a sufficient accuracy.

As previously pointed out, the development of new contact materials like metal silicides has reinforced the need for an accurate evaluation of parasitics in order to extract meaningful values of ρ_c . In fact, in this case, the atomically clean contact interfaces allow one to obtain values of ρ_c lower by more than one order of magnitude with respect to the Al films. For this particular type of metallizations the extraction of accurate values of contact resistivity looks quite problematic and, although consistent results can be obtained by using the TLTR, the sources of error caused by the indirect measurement method in this technique are not negligible (compare, e.g., the intercept of the two lines plotted in fig. 12: it is very difficult to state if the difference between the intercepts is due to a real difference in contact resistance, or to measurement error). Above all, for high values of the sheet resistance, the determination of the front resistance from the measured data is particularly sensitive to small variations in the separation distance between the contacts. In the case of a small contact resistivity, even negative values of the front resistance can be found.

For low-resistive contacts, other techniques, based on test structures incorporating a single contact, are at least in principle preferable to the TLTR and will be described in the following. Before doing this, let us however examine a different version of the transmission line resistor, namely the circular transmission line resistor, that, although not of particular interest for contacts on Si substrates, has been widely used in the characterization of metal systems on gallium arsenide.

3.4. The circular transmission line resistor (CTLR)

The circular transmission line resistor has been introduced by Reeves in ref. [84] with the purpose of simplifying the technological steps required to fabricate test patterns for the determination of ρ_c .

The implementation of the in-line TLTR geometry necessitates a two- or three-mask process, depending on the contact configuration. In particular, in GaAs, a mesa etch is required to isolate the epitaxial or ion-implanted layers. By using the test structure shown in fig. 7, consisting of a transmission line resistor of circular symmetry, this step can be eliminated, thus simplifying the fabrication procedure. When measuring the resistance between the central dot and the inner ring contact, or between the two ring contacts, in fact, all the current is confined and flows uniformly from the positive to the negative terminal, because of the inherent self-isolation of the circular symmetry.

From the cross section of the test structure shown in fig. 20, the resistances R_1 and R_2 measured between the two inner and outer contact, respectively, can be written as

$$R_1 = R_A + (R_{C0} + R'_{C1}), \quad (3.16a)$$

$$R_2 = R_B + (R_{C1} + R_{C2}). \quad (3.16b)$$

In order to derive ρ_c from these measurements, the usual resistor network applied to analyze the TLTR has been modified by Reeves to take into account the circular geometry. The basic transmission line equations have then been solved by maintaining the distinction between R_{sh} and R_{sk} . Since we have two unknown parameters, ρ_c and R_{sk} , the end resistance R_e of the central contact needs also to be measured. By introducing R_e in the calculations, the following equation is finally derived

$$\left[\ln\left(\frac{r'_2}{r_1}\right) R_1 - \ln\left(\frac{r'_1}{r_0}\right) R_2 \right] (R_e)^{-1} = \left[\ln\left(\frac{r'_2}{r_1}\right) \left(\frac{E(r_0)}{\alpha r_0} + \frac{1}{\alpha r'_1} \frac{A(r_1, r'_1)}{C(r_1, r'_1)} \right) \right. \\ \left. - \ln\left(\frac{r'_1}{r_0}\right) \left(\frac{1}{\alpha r_1} \frac{B(r_1, r'_1)}{C(r_1, r'_1)} + \frac{1}{\alpha r'_2} \frac{A(r_1, r'_1)}{C(r_1, r'_1)} \right) \right] \left(\frac{A(r_1, r'_1) B(r_1, r'_1)}{C(r_1, r'_1)} + D(r_1, r'_1) \right)^{-1}, \quad (3.17)$$

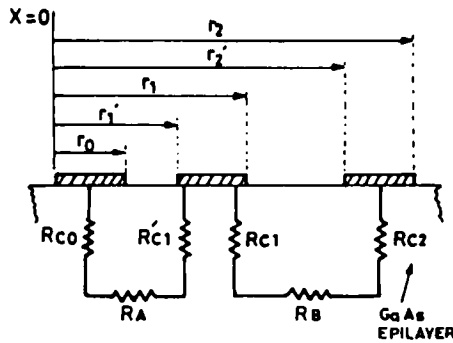


Fig. 20. Cross section of a circular transmission line contact pattern. From ref. [84].

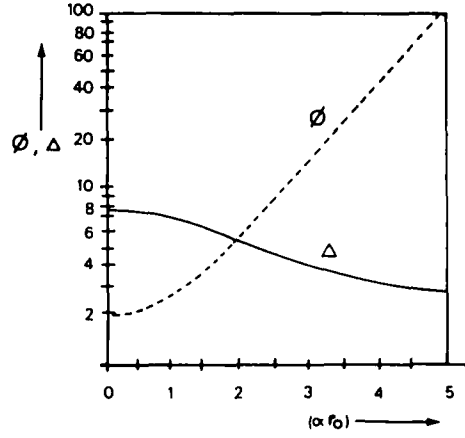


Fig. 21. The dependence of ϕ and Δ on the parameter αr_0 . From ref. [84].

where α is the attenuation constant, defined as the inverse of the transmission length l_t , and A , B , C , D and E are convenient combinations of the modified Bessel functions of the first and second kind:

$$A(r, x) = I_1(\alpha r)K_0(\alpha x) + I_0(\alpha x)K_1(\alpha r),$$

$$B(r, x) = I_1(\alpha x)K_0(\alpha r) + I_0(\alpha r)K_1(\alpha x),$$

$$C(r, x) = I_1(\alpha r)K_1(\alpha x) - I_1(\alpha x)K_1(\alpha r),$$

$$D(r, x) = I_0(\alpha x)K_0(\alpha r) - I_0(\alpha r)K_0(\alpha x),$$

$$E(r, x) = I_0(\alpha r)/I_1(\alpha r).$$

For a given test configuration, the rhs of eq. (3.17), named ϕ , is calculated and plotted as a function of αr_0 (see fig. 21), whereas the lhs is determined experimentally. From $\text{lhs} = \phi$, the value αr_0 is determined, and hence α can be found. Finally, ρ_c can be determined directly from the following equations:

$$\rho_c = \left[\ln\left(\frac{r'_2}{r_1}\right) R_1 - \ln\left(\frac{r'_1}{r_0}\right) R_2 \right] (r_0)^2 \Delta, \quad (3.18a)$$

where

$$\Delta = \frac{2\pi}{(\alpha r_0)^2 \phi} \left(\frac{A(r_1, r'_1)B(r_1, r'_1)}{C(r_1, r'_1)} + D(r_1, r'_1) \right)^{-1}. \quad (3.18b)$$

Contact resistance measurements were performed in ref. [84] on test patterns of both circular symmetry and in-line geometries, prepared on epitaxial GaAs layers. The contacts were conventional Au-Ge-Ni, with a final Au metallization, leading to a total thickness of 200 nm, to provide equipotential metal layers. An average $\rho_c = 6.8 \times 10^{-5} \Omega \text{ cm}^2$ was measured in the CTLR, in excellent agreement with the average value of $6.6 \times 10^{-5} \Omega \text{ cm}^2$ derived on the in-line geometry.

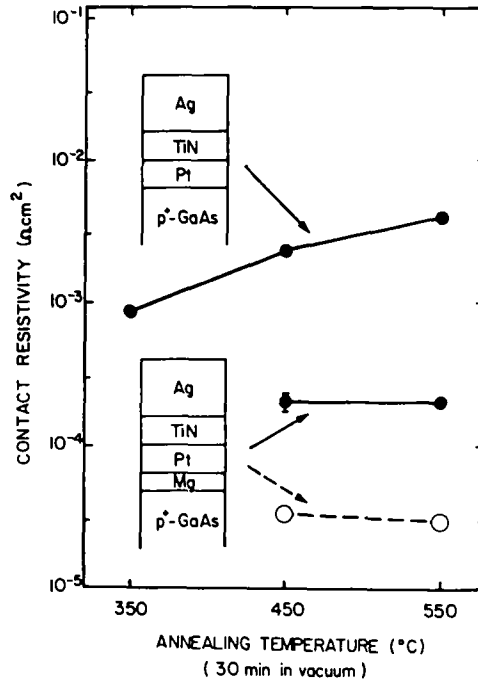


Fig. 22. Contact resistivity of Ag/TiN/Pt/GaAs(p) and Ag/TiN/Pt/Mg/GaAs(p) systems as a function of annealing temperature. Solid circles and solid lines represent true values of contact resistivity. Open circles and dashed lines are the contact resistivity values for the Ag/TiN/Pt/Mg/GaAs(p) system calculated without taking the modified sheet resistance value into account. From ref. [85].

Contact resistivity measurements on test patterns conforming to the circular transmission line model have been reported in ref. [85]. Laterally uniform contacts to p-type GaAs were formed by solid-phase reaction of Pt. In order to avoid finite metal sheet resistance contributions, thick Ag overlayers were deposited on the contacts, with a TiN layer in between preventing the reaction of Pt with Ag. End resistance measurements were also carried out. A ratio $R_{sk}/R_{sh} \approx 1$ was determined, showing that the reaction between Pt and GaAs does not modify the resistance of the doped layer significantly. In contrast, in the case of a thin (100 Å) layer of Mg interposed between GaAs and Pt, a drop in R_{sk} by more than a factor of six was observed, possibly resulting from the doping action of Mg. The expected differences in doping concentration are reflected in the values of contact resistivity, reported as solid circles in fig. 22. It is interesting to note that, in the case of the contact incorporating Mg, substantially lower values of ρ_c (open circles) would have been derived assuming no change in R_{sk} , with respect to those calculated with the modified sheet resistance. The discrepancy between the two types of approach is expected to be substantial in metallization systems containing dopant elements.

4. Four-terminal single-contact Kelvin resistors: the cross Kelvin resistor (CKR)

4.1. One-dimensional model and first experimental results

The so-called D-type cross Kelvin resistor, shown in fig. 8, is a four-terminal test structure that allows a direct measurement of the interfacial Kelvin resistance. This is defined as the ratio

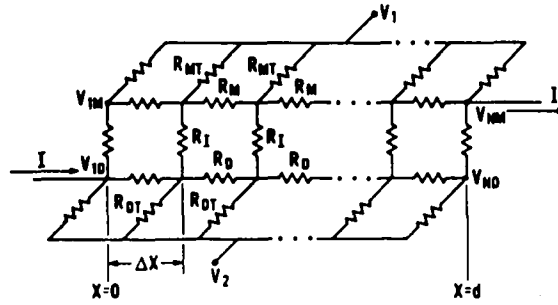


Fig. 23. Resistor network model of the four-terminal test structure. From ref. [57]. © 198-IEEE.

between the voltage V_i monitored at the two voltage taps (1 and 2) which are orthogonal to the direction of the current flow and the current I flowing through two lined-up arms (from 4 to 3). The measured voltage represents the voltage drop across the interfacial layer, except for the contributions related to the parasitic area around the contact, which will be discussed in detail in the following, and apart from the vertical voltage drop in the diffusion layer, which is typically considered negligible, since most of the current flows very close to the interface, where the doping concentration is higher. In comparison to the TLTR, the real advantage of this structure is the direct measurement of the contact resistance on a single contact.

A resistor of similar topology has been used by McNeil [86], Shih and Blum [87] and Anderson and Reith [35]. However, only recently models have been developed to relate the measured contact resistance to the contact resistivity in the case of a homogeneous metal/semiconductor interfacial layer, what has made the use of this test structure particularly attractive for applications in VLSI contacts. A 1-D model has been presented in ref. [57]. As shown in fig. 23 the model is based on a transmission line network consisting of N metal resistors R_M , diffusion resistors R_D , and interfacial resistors R_I , where $N = d/\Delta x$ and d is the contact window length, whereas Δx is the incremental length. The metal and diffusion taps used for monitoring the voltage are also included and are represented by the resistors R_{MT} and R_{DT} , respectively. As stressed before, the model is based on the assumption of a uniform interfacial layer, this implying that the resistors R_I are identical.

By applying standard circuit laws, the following equation can be shown to hold:

$$R_i = (V_2 - V_1)/I = \rho_c/wd, \quad (4.1)$$

where R_i is the so-called interfacial resistance while, following the previous definitions, d and w are the contact length and width, respectively.

Test results obtained with Al and Al-Si metallizations on low-resistance Si diffused layers ($R_{sh} = R_{sk} = 6 \Omega/\square$) are presented in fig. 24, where the measured values of interfacial contact resistance are plotted as a function of the contact window area. From the data relative to the Al-Si contacts one can obtain from eq. (4.1) the value of ρ_c , which in this case is equal to 3.2×10^{-6} and $1.4 \times 10^{-6} \Omega \text{ cm}^2$, depending on the sintering temperature (425 and 500 °C, respectively). These results are in agreement with the values typically reported for this type of metallization. On the other hand, in the case of pure Al, the relation between R_i and the contact area is not linear, as might be expected because of the presence of non-uniformities at the interface, mainly located at the perimeter of the contact, and caused by silicon dissolution into the aluminum during the sintering process. Similar results from the same type of metallization were observed in ref. [88].

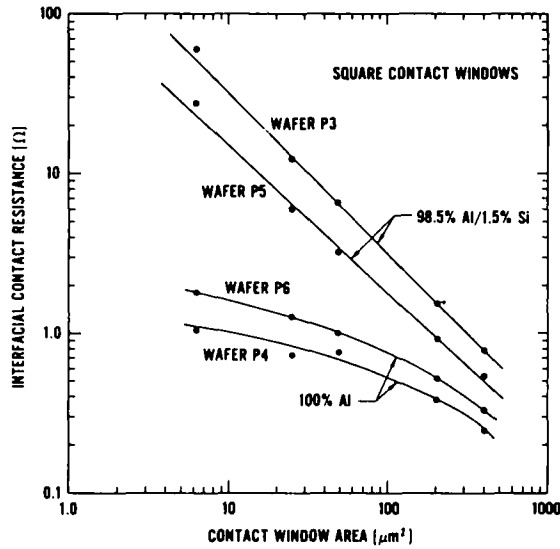


Fig. 24. Measured interfacial contact resistance R_i versus area for four-terminal Kelvin structures. Wafers P3 and P5 have Al-1.5% Si metallization and were sintered for 20 min at 425 and 500 °C, respectively. Wafers P4 and P6 have 100% Al metallization and were sintered for 20 min at 425 and 500 °C, respectively. From ref. [59]. © 198-IEEE.

In this case, the contact can only be characterized by the value of the interfacial contact resistance. As a consequence the experimental data cannot be used to accurately predict the interfacial resistance of a contact with a different window area.

In order to derive a reliable value of ρ_c , measuring on a single contact area is not sufficient. Several (at least three) test structures with different contact areas are required to test the validity of the experimental approach through the slope equal to -1 in the plot of R_i versus contact area.

4.2. Two-dimensional current flow

The CKR structure has been later applied to the determination of the contact resistivity in silicon/silicide interfaces (TiSi_2 , Pd_2Si , NiSi) on phosphorus- and boron-doped layers, of sheet resistance $R_{sh} = 4$ and $85 \, \Omega/\square$, respectively [28,29,89]. After metal evaporation and patterning, by lift-off, the silicides were formed by thermal annealing in a vacuum furnace. An aluminum film was then deposited on top of the silicide and patterned, to provide an equipotential metal layer. In all cases, notwithstanding the expected uniformity of the interface, it was found that the contact resistivity calculated from eq. (4.1) depends on the contact area, as shown in table 3 for the different silicides. A sublinear behaviour of the interfacial resistance versus contact area, instead of the expected linear behaviour of fig. 24, has been found also by Maddox [90] and Ford [91].

A more detailed analysis of the test structure shows in fact an important source of error, as predicted, from a qualitative point of view, in ref. [59]. Similarly to the TLTR case, it consists of the parasitic resistive drops that result from the width of the diffused area being larger than the sides of the contact window. The effect is even worse here because of the lateral diffusion of the dopant, during the prolonged thermal treatment at high temperature, which contributes to a further increase in the actual width of the diffused region. As shown in fig. 25 the area around the contact introduces a parasitic resistance contribution which is sensed in the y direction,

Table 3

	Contact dimensions (μm^2)	ρ_c ($\Omega\text{ cm}^2$)		
		experimental	extracted	TLM
Al/Pd ₂ Si/n ⁺ -Si	20 × 20	$(4.1 \pm 0.9) \times 10^{-7}$	7×10^{-8}	—
	10 × 10	$(2.7 \pm 1.1) \times 10^{-7}$		
	5 × 5	$(1.5 \pm 0.9) \times 10^{-7}$		
Al/NiSi/n ⁺ -Si	20 × 20	$(3.8 \pm 1.8) \times 10^{-7}$	5×10^{-8}	—
	10 × 10	$(1.2 \pm 0.3) \times 10^{-7}$		
	5 × 5	$(0.9 \pm 0.3) \times 10^{-7}$		
Al/TiSi ₂ /n ⁺ -Si	20 × 20	$(4.4 \pm 0.9) \times 10^{-7}$	8×10^{-8}	2×10^{-7}
	10 × 10	$(2.3 \pm 0.4) \times 10^{-7}$		
	5 × 5	$(1.7 \pm 0.2) \times 10^{-7}$		
Al/Pd ₂ Si/p ⁺ -Si	20 × 20	$(8.6 \pm 0.8) \times 10^{-6}$	3×10^{-6}	6×10^{-6}
	10 × 10	$(5.3 \pm 0.9) \times 10^{-6}$		
	5 × 5	$(6.0 \pm 1.3) \times 10^{-6}$		
Al/NiSi/p ⁺ -Si	20 × 20	$(3.6 \pm 0.8) \times 10^{-5}$	2×10^{-5}	3×10^{-5}
	10 × 10	$(2.5 \pm 1.1) \times 10^{-5}$		
	5 × 5	$(2.4 \pm 1.1) \times 10^{-5}$		
Al/TiSi ₂ /p ⁺ -Si	20 × 20	$(7.9 \pm 0.4) \times 10^{-5}$	7×10^{-5}	6×10^{-5}
	10 × 10	$(6.4 \pm 0.8) \times 10^{-5}$		
	5 × 5	$(7.8 \pm 0.8) \times 10^{-5}$		

whereas an additional parasitic effect in the x direction is due to the current flowing laterally at the sides of the contact (I_1 and I_3 in fig. 25). Such a parasitic effect has been first discussed from a quantitative point of view in refs. [28,89].

The computer model developed for this purpose has been previously described in section 3. By solving numerically the standard circuit laws, the voltage drop V between the lateral pad and the metal surface can be calculated for given ρ_c , R_{sh} and R_{sk} values, contact geometry and tolerance. The resulting voltage drop is then used to derive the contact resistance R_i^* , i.e. the resistance we would expect to measure in the pattern under test. By the product R_i^*A , where A is the contact area, the apparent contact resistivity ρ_c^* can be determined, which differs from ρ_c

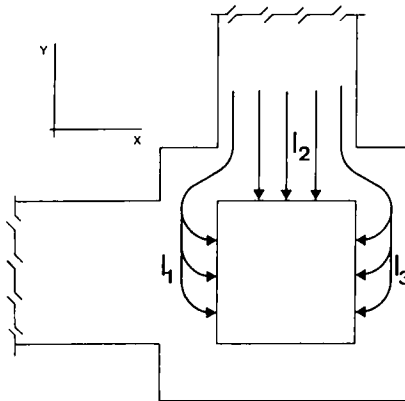


Fig. 25. Lateral current crowding in the CKR.

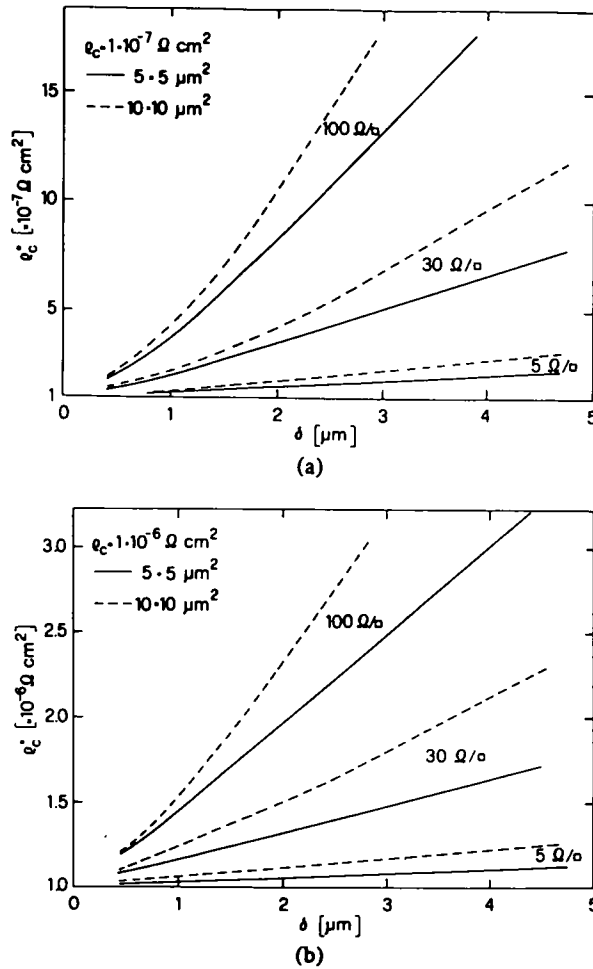


Fig. 26. Apparent contact resistivity ρ_c^* versus tolerance δ , for different contact areas and sheet resistances, and (a) $\rho_c = 1 \times 10^{-7} \Omega \text{ cm}^2$, (b) $\rho_c = 1 \times 10^{-6} \Omega \text{ cm}^2$. From ref. [73]. © 198-IEEE.

because of the lateral current crowding effects. As an example, figs. 26a and 26b show the values of ρ_c^* versus tolerance for typical R_{sh} , R_{sk} and d , and for ρ_c equal to 1×10^{-7} and $1 \times 10^{-6} \Omega \text{ cm}^2$, respectively. It can be seen that the errors are quite significant for $\rho_c = 10^{-7} \Omega \text{ cm}^2$ and $R_{sh} = R_{sk} = 100 \Omega/\square$, and in the direction of overestimating the contact resistivity. Errors of about one order of magnitude are to be expected for $d = 5 \mu\text{m}$ and $\delta = 2 \mu\text{m}$, while a much lower overestimate (on the order of 100%) is predicted in the case of $\rho_c = 1 \times 10^{-6} \Omega \text{ cm}^2$. Moreover, the extent of the error is appreciably reduced by lowering the diffused layer sheet resistance from 100 to $5 \Omega/\square$.

The theoretical results are consistent with the observation that the potential drop produced in the parasitic area by the lateral current crowding is much less than the voltage drop across the metal/semiconductor interface, and thus $\rho_c^* = \rho_c$. As the contact resistivity decreases, however, the potential across the contact interface correspondingly decreases to a negligible value, and the parasitic contribution completely dominates the measured Kelvin potential. Under these conditions, ρ_c^* becomes independent of ρ_c . Similar results have been achieved in

refs. [92,93], where the minimum values of contact resistivity which can be extracted in this type of test structures have been extensively analyzed, as a function of the geometrical and technological parameters.

The curves in fig. 26 demonstrate that lateral current crowding effects have to be taken into account in the determination of very low contact resistivity values like, for example, the ones obtainable in heavily doped silicon/silicide interfaces, to avoid a strong overestimate of ρ_c . On the other hand, the observation that lateral crowding does not affect appreciably contact resistivity measurements in the case of ρ_c values equal to or higher than $10^{-6} \Omega \text{ cm}^2$, and low sheet resistances and tolerances, is in agreement with the experimental results obtained in refs. [57,60,94].

The application of the model to the experimental data presented in table 3 allows one to determine, for each contact metallization, a value of contact resistivity which is independent of the particular contact geometry under test. The extracted values of contact resistivity are also reported in table 3. It can be observed that, for all the silicides under investigation, the values are appreciably lower than the ones typically measured for the Al metallizations, further confirming the versatility of these materials for very large scale integration contacts. Finally, table 3 reports also the contact resistivity extracted from test patterns conforming to the transmission line model. Good agreement has been achieved for the two types of measurement, especially for high contact resistances.

It is worthwhile to remind that the 2-D approach has been applied in ref. [95] in an attempt to fit the experimental data relative to pure Al, reported in fig. 24. The lateral current crowding alone, however, was not sufficient to explain the observed behaviour. Possible modifications in R_{sk} , on the order of 50%, were also shown to play a minor role. The discrepancy between theoretical and experimental data was thus mostly attributed to the horizontal-vertical current flow induced by the heavy pitting, which cannot be easily modelled.

A very accurate analysis of the cross Kelvin resistor, from both theoretical and experimental points of view, has been carried out by Loh et al. [32,61,62], and subsequently extended by Scorzoni and Finetti in ref. [63]. In this case the CKR structure under study is slightly different from the previous one, since the width of the current and voltage taps is $w = d + 2\delta$, whereas in the previous case w was equal to d (compare the test structures in figs. 8 and 27 known as D- and L-resistors, respectively).

CKR test structures of several contact sizes have been prepared [32,62]. In this case the metallization usually consisted of three films: the contact metal, such as a self-aligned silicide, obtained for example by Pt deposition on polysilicon followed by a thermal treatment in N_2 , or LPCVD tungsten; the barrier layer to prevent metal-silicon interdiffusion; on top, a low-resis-

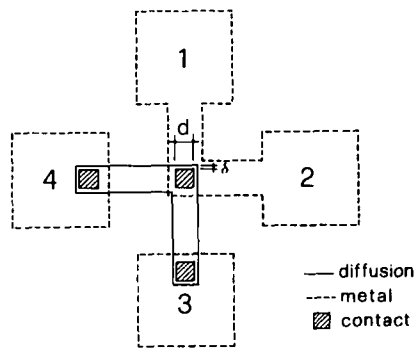


Fig. 27. The L-type cross Kelvin resistor (CKR).

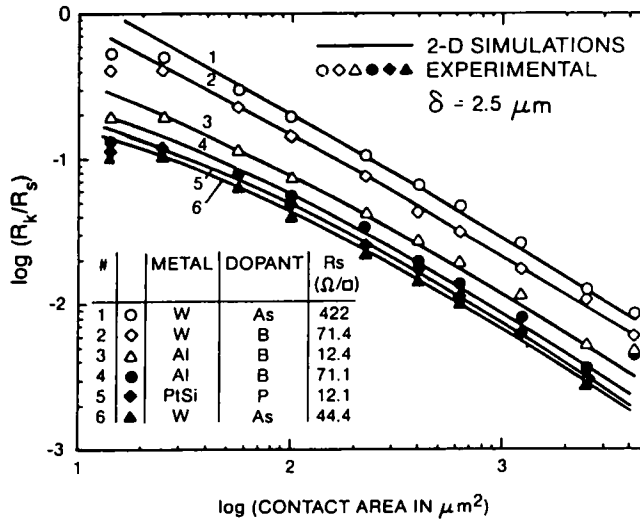


Fig. 28. The ratio of Kelvin contact resistance to diffusion sheet resistance plotted as a function of the contact area for different transfer length l_t for CKR with overlap being $2.5 \mu\text{m}$. Symbols denote measured data; solid lines are 2-D simulations. The results are summarized in table 4. From ref. [32]. © 198-IEEE.

tivity Al-Si film to ensure an equipotential metal surface. In fig. 28 the ratio of the interfacial contact resistance R_i (here named R_k) to the sheet resistance of the diffused layer R_s is shown as a function of the contact area, whereas δ is maintained constant at $2.5 \mu\text{m}$. Partially in analogy to the 1-D case, the experimental results are plotted as the logarithm of the ratio between the interfacial Kelvin resistance and the sheet resistance versus logarithm of the contact area. The data can then be fitted by using the transmission length l_t as an independent parameter for a specified test structure geometry. From fig. 28, it can be observed again, as expected, a large deviation from the 1-D model as l_t is decreased (going from curve 1 to curve 6) and for increasing contact windows, due to the increasing parasitic component caused by current crowding effects. The 2-D simulations however are able to fit in an excellent way the experimental results over a wide range of contact areas, and this allows the accurate extraction of different l_t for the metal (W, Al, PtSi) to n^+/p^+ (B, P, As) diffusions. The results are summarized in table 4. The contact resistivity can then be derived since the value of R_s is known. It must be underlined here, however, that this procedure is particularly useful and accurate if the contact resistivity underneath the contact is not modified by reactions of metal with silicon, as it is expected to be in this particular case, where for example the silicon consumption underneath the contact was minimized by using a very thin Pt layer. The influence of $R_{sh} \neq R_{sk}$ will be examined in detail in section 4.4.

Table 4 ^{a)}

Number	Metal	Dopant	R_s (Ω/□)	l_t (μm)	ρ_c (Ω μm ²)
1	W	As	422	3.5	3500
2	W	B	71.4	2.75	540
3	Al	B	12.4	1.4	24.3
4	Al	B	71.1	0.9	57.6
5	PtSi	P	12.1	0.65	5.11
6	W	As	44.4	0.5	11.1

^{a)} From ref. [32]. © 198-IEEE.

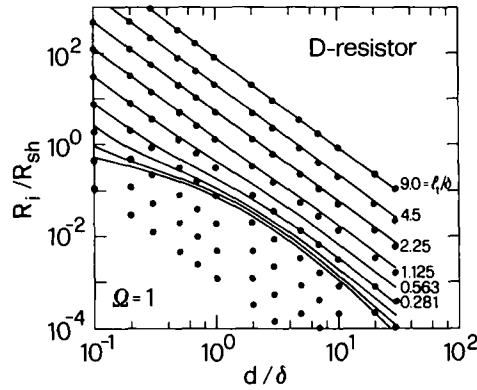


Fig. 29. Generalized extraction curves (solid lines) for a square-contact D-type CKR. The parameter l_t/δ is in octave steps and $\Omega = 1$. For comparison, 1-D calculations [57] are reported as dots.

Similarly to the TLTR case discussed in section 3.2, generalized extraction curves can be derived for the D- and L-resistors. This work was first carried out by Loh et al. on L-resistors with a finite-element model [32,61,62]. Similar calculations have been performed by Scorzoni et al. [63,96] for the two types of resistors using the model described in section 3.2. Fig. 29 reports the comparison between the numerical simulations and the 1-D model for the D-resistor with a square central contact, showing a large discrepancy at low l_t/δ ratios.

In a recent paper, Chalmers and Streetman [97] stressed that, in order to use the generalized extraction curves, the geometries of the structure in the contact area must be known, and in particular the difference in the contact window size and the diffusion region δ must be known to a precision better than a transfer length. When the dopant lateral diffusion approaches or exceeds a transfer length, its effect must be considered in order to accurately determine ρ_c . Computer simulations indicate that this is accomplished if the diffusion width is considered to extend to the point where the sheet carrier concentration has decreased to 40% of the value in the original diffused region.

In most practical cases a further source of error originates from the misalignment of the contact window with respect to the diffused area. The extent of this effect will be examined in section 6.2 in the case of the six-terminal cross Kelvin resistor.

Finally, it should be observed that the values of contact resistivity obtainable using metal silicides can be in the range 10^{-8} – 10^{-7} Ω cm² for sufficiently high doping levels, in agreement with the results presented in ref. [28] for different silicide preparation procedures. This is a further confirmation that pessimistically high values of contact resistance have been predicted for the VLSI contacts of future generations because the values of ρ_c were very grossly overestimated.

4.3. Comparison between D- and L-resistors

While the difference in the layout of the two resistors does not appear remarkable, Gillenwater et al. [93] have shown that the minimum extractable contact resistivity, ρ_{cmin}^* (or ρ_{ce}^{min}), can be significantly lower in the test structure in fig. 8 (D-resistor) with respect to the one in fig. 27 (L-resistor) for devices of the same contact size and alignment tolerance. For the sake of clarity, it must be emphasized that ρ_{cmin}^* represents the value of the apparent contact resistivity ρ_c^* as $\rho_c \rightarrow 0$, that is in the conditions where the potential in the semiconductor completely dominates the measured Kelvin potential.

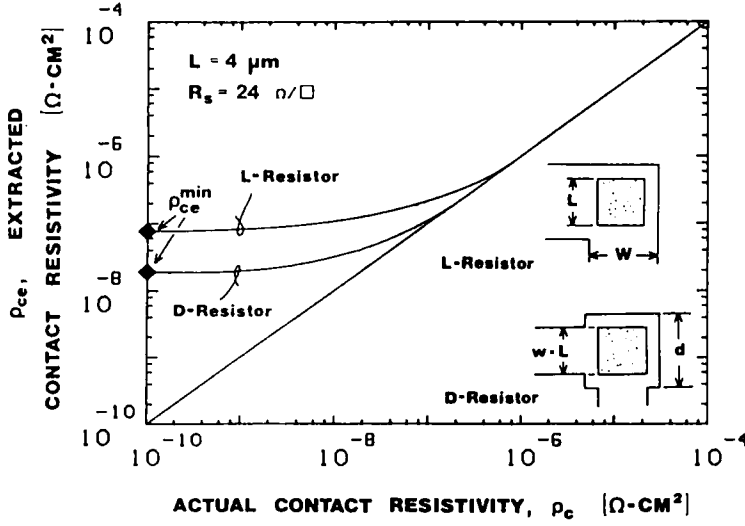


Fig. 30. Typical ρ_c^* curves for similar L- and D-resistor devices. D-resistor: $L = 4 \mu\text{m}$, $w = 4 \mu\text{m}$, $d = 5.7 \mu\text{m}$. L-resistor: $L = 4 \mu\text{m}$, $w = 5.7 \mu\text{m}$. From ref. [93]. © 198-IEEE.

The 2-D simulations performed by the authors were based on a finite-differences approximation of eqs. (2.11) and (2.12) similar to that described in section 3.2. Fig. 30 reports the minimum extractable contact resistivity as a function of the real contact resistivity for a given contact size and tolerance in L- and D-resistors. As the measured value of ρ_c^* approaches $\rho_{c\min}^*$, the error in the correctly extrapolated value of ρ_c becomes very large, since different contact resistivities (for example all the values in the range 10^{-10} to $10^{-9} \Omega \text{cm}^2$) can provide identical values of apparent contact resistivity, thus strongly reducing the sensitivity of the CKR.

The physical explanation for the different behaviour can be found in the sensed voltage being an average of the transverse potential distribution. For low l_t/δ , in fact, only the leading edge of the contact (with respect to the current flow) gives a measurable voltage; in the L-resistor an additional contribution to the contact potential is sensed, due to the current flowing in the parasitic area in front of the contact, whereas in the D-resistor this phenomenon is less accentuated.

The generalized extraction curves are reported in figs. 29 and 31 (solid lines) for the D- and L-resistor, respectively. A noticeable difference, as we remarked above, can be observed

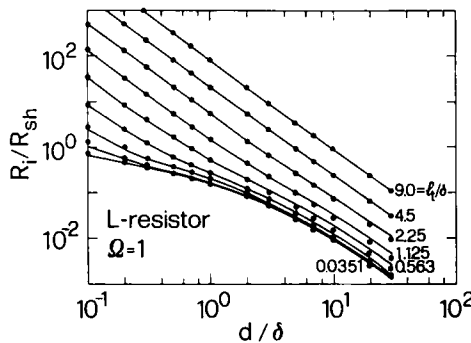


Fig. 31. Generalized extraction curves (solid lines) for a square-contact L-type CKR. The parameter l_t/δ is in octave steps and $\Omega = 1$. For comparison, 2-D analytical calculations from thin film model [98] are reported as dots.

between the two types of resistors. In fact, for small values of l_t/δ , the D-resistor shows a greater resolution in the interfacial resistance with respect to the L-resistor. This better sensitivity has, as a major drawback, the need to sense appreciably lower resistances.

4.4. Sheet resistance modification effects

Until now, we have not taken into account the effect of possible sheet resistance modifications underneath the contact [63]. While this problem does not concern metal silicides deposited directly on silicon, appreciable sheet resistance modifications can occur in the case of silicides formed by thermal reactions. Therefore it is of interest for the users of graphic aids like figs. 29 and 31 to realize to what extent the extraction of ρ_c is influenced by differences between R_{sh} and R_{sk} .

Referring to the generalized scaling theory presented in section 2.5, for the cross Kelvin resistor we can write

$$\frac{R_i}{R_{sh}} = \frac{R_i}{R_{sh}} \left(\frac{d}{\delta}, \frac{l_t}{\delta}, \Omega \right), \quad (4.2)$$

where the symbols have their usual meaning.

By means of the pseudo-three-dimensional simulation program described in section 3.2, and using (4.2), we have generated the plots of figs. 32a and 32b and 33a and 33b reporting as solid lines the generalized curves calculated for $\Omega = 3$ and $1/3$, for the D- and L-resistors, respectively. These curves can be very useful in order to determine the effect of $R_{sk} \neq R_{sh}$ on the extraction of ρ_c when the extent of the deviation of R_{sk} from R_{sh} is not known. In fact to our knowledge (at least for silicon devices) no Ω value outside the interval $[1/3, 3]$ has been reported in the literature; consequently $\Omega = 1/3$ and $\Omega = 3$ can be considered the minimum and the maximum physical limits between which the real Ω can vary.

Once the values of resistance R_i , sheet resistance R_{sh} and geometries d and δ are known, it is easy to estimate from figs. 32 and 33 the maximum and minimum value of ρ_c compatible with the assumption that $1/3 < \Omega < 3$. As an example, in the case of the L-resistor, if $R_i = 10 \Omega$, $R_{sh} = 20 \Omega/\square$, $d = 1 \mu\text{m}$ and $\delta = 1 \mu\text{m}$, then $0.29 < l_t < 1 \mu\text{m}$; finally, according to the relation

$$\rho_c = l_t^2 R_{sk} = \Omega l_t^2 R_{sh}, \quad (4.3)$$

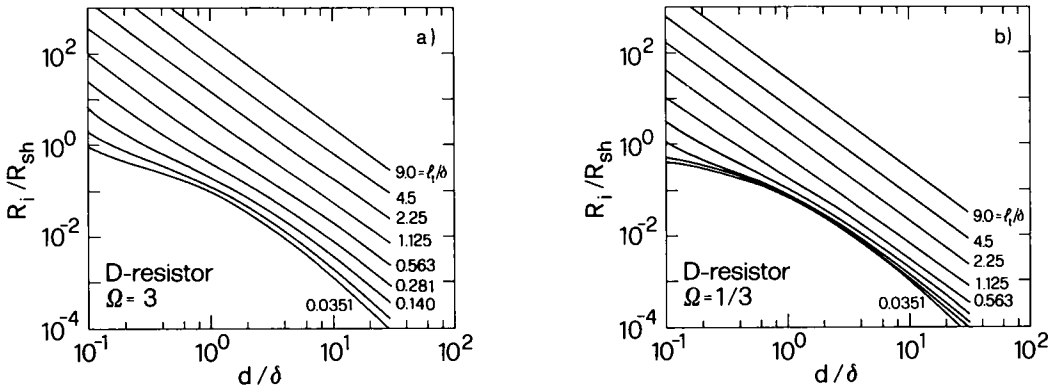


Fig. 32. Generalized extraction curves (solid lines) for a square-contact D-type CKR in the cases $\Omega = 3$ (a) and $\Omega = 1/3$ (b). The parameter l_t/δ is in octave steps.

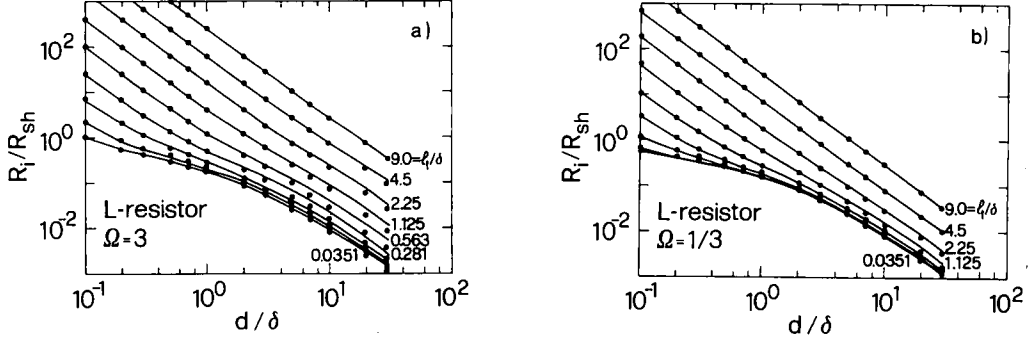


Fig. 33. Generalized extraction curves (solid lines) for a square-contact L-type CKR in the cases $\Omega = 3$ (a) and $\Omega = 1/3$ (b). The parameter l_1/δ is in octave steps. For comparison, 2-D analytical calculations from an extended thin film model [100] are reported as dots.

we have $5.0 \times 10^{-8} < \rho_c < 6.7 \times 10^{-8} \Omega \text{ cm}^2$ with a “central” value $\rho_c = 6.3 \times 10^{-8} \Omega \text{ cm}^2$ obtainable from fig. 31. In this case the maximum error on the extraction of ρ_c is 20%.

It can be easily verified that the error increases if the values of ρ_c and R_{sh} are fixed to the same “central” value as before and the dimensions d and δ are increased: if $d = 5 \mu\text{m}$ and $\delta = 2.5 \mu\text{m}$, we have $3 \times 10^{-8} < \rho_c < 1.2 \times 10^{-7} \Omega \text{ cm}^2$, and the error calculated with respect to $\rho_c = 6.3 \times 10^{-8} \Omega \text{ cm}^2$ can be up to 100%. The observed correlation between error magnitude and the contact geometry is in agreement with the fact that by reducing the contact area, the resistance contributions of the contact interface tend to become dominant with respect to the parasitic effects, approaching the one-dimensional case. Similar behaviour has already been observed in the case of the contact window misalignment, thus confirming that the use of reduced contact geometries minimizes the error magnitude on ρ_c evaluation.

4.5. Analytical models

Very recently two analytical models have been published, able to predict quantitatively the effect of the current flowing in the overlap region between the contact edge and the diffusion sidewall of a L-resistor. In the work by Schreyer and Saraswat [99] a variational technique has been applied, and the following formula has been calculated by minimizing the power dissipation of the system:

$$R_i = \frac{\rho_c}{l_x l_y} + \frac{4R_s \delta^2}{3W_x W_y} \left(1 + \frac{\delta}{2(W_x - \delta)} \right), \quad (4.4)$$

where l_x and l_y are the contact length and width, respectively, and W_x and W_y are the widths of the voltage and current taps, respectively, and the other symbols have their usual meaning. The comparison between numerical simulations and analytical derivations shows good agreement for both high and low values of ρ_c . In the range where the two terms of eq. (4.4) are approximately equal, however, a slight disagreement can be observed and other types of simulation are preferable.

A different approach to the problem has been considered by Lienweg and Hannaman [98]. The basic idea of the so-called thin film model (TFM) is to replace the original contact area with: (a) an equipotential core zone of smaller dimensions than the contact and embedded in the semiconducting layer modelled as a two-dimensional sheet; and (b) a lumped resistor with a

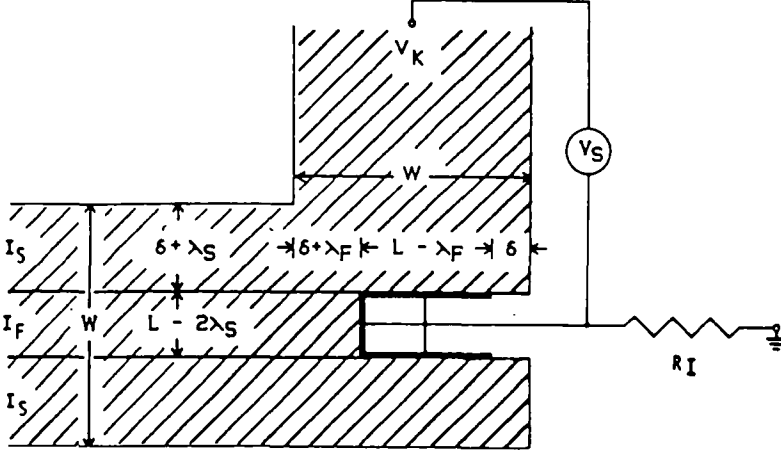


Fig. 34. TFM of a L-type CKR. The square contact has been replaced by an equipotential core of reduced dimensions, embedded in the lower semiconducting sheet (cross-hatched), and a lumped resistor representing the interfacial resistance. Current is injected at the left, far from the contact. In the text the contact length (and width) L is named d .
From ref. [98]. © 198-IEEE.

value equal to the ideal interfacial resistance and connected to the core region (see fig. 34). Very good agreement with the numerical simulations has been achieved for a large range of d/δ and l_v/δ values, as one can see comparing the dots (TFM) and the solid lines (numerical) of fig. 31. The TFM has been extended [100] in order to take into account possible differences between R_{sh} and R_{sk} . It can be shown that

$$\frac{R_i}{R_{sh}} = \frac{1}{\pi} \operatorname{arccosh}\left(\frac{1-t}{a}\right) \frac{\delta + \lambda_s}{w} + \Omega \frac{(l_v/\delta)^2}{(d/\delta)^2}, \quad (4.5)$$

where

$$\frac{\delta + \lambda_s}{w} = \frac{1 + 1/(S-1)}{T}, \quad T = \frac{d}{\delta} + 2, \quad S = \frac{T}{(l_v/\delta)\Omega V}, \quad V = \left[\operatorname{tgh}\left(\frac{d/\delta}{l_v/\delta}\right) \right]^{-1} - \frac{l_v/\delta}{d/\delta}$$

and $a > 0$ and $t < 0$ are determined from the transformation

$$q(x) = \operatorname{arccosh}[(b-2x)/b] + (b-1)^{1/2} \arccos[(bx+b-2x)/b(1-x)],$$

which maps

$$q_1 = \pi \frac{T - \{1 + (1/S)[d/\delta - 2/(S-1)]\}}{1 + 1/(S-1)}, \quad q_2 = \pi \frac{1}{1 + 1/(S-1)}$$

in $x_1 = t - a$ and $x_2 = t + a$.

With this notation it is easy to verify that the solution (4.5) follows the generalized scaling rule of eq. (4.2).

Figs. 33a and 33b report the comparison between numerical simulations (solid lines) and analytical derivations (dots) in the cases $\Omega = 3$ and $1/3$, respectively. Besides the excellent

agreement already underlined in the case $\Omega = 1$, good agreement can also be found when $R_{sk} \neq R_{sh}$. The fitting is not good enough only for $\Omega = 3$ and $d/\delta > 2$, probably because in this case the schematization of the contact in the TFM is too drastic.

The TFM was implemented to fit a contact resistivity $\rho_c = (51.8 \pm 2.9) \times 10^{-8} \Omega \text{ cm}^2$ on six-terminal structures (see section 6) with Au–Ge–Ni contacts in n^+ implanted Si–GaAs [98]. The contact size varied between 1.2 and 9.7 μm , the flange width δ between 0.75 and 3.25 μm and the sheet resistance (measured independently and supposed to be such that $R_{sh} = R_{sk}$) was 353 Ω/\square .

Finally, it can be shown that, while the TFM fits quite well the L-CKR resistance values, the fitting with the D-resistor is good only for large l_t/δ or for small d/δ values.

4.6. Optimization of the test structure

Based on the previous observations, and following ref. [93], a few considerations are suggested to reduce the errors in CKR structures:

- (1) The length of the voltage sensing arms should be at least twice the diffusion width. In fact, at this distance, the potential is found to vary less than 1% in the y direction for all the devices investigated.
- (2) The parasitic area around the contact must be minimized, by keeping to a minimum the alignment tolerances.
- (3) The D-resistor should be preferred to the L-resistor.
- (4) As we will see in more detail in section 6.3, contact misalignment should be minimized.
- (5) The diffusion sheet resistance should be as low as possible.
- (6) Rounding of the contacts and diffusion areas should be avoided by proper etching procedures, otherwise lateral current crowding would be further enhanced.

5. Four-terminal single-contact Kelvin resistors: the contact end resistor (CER)

5.1. Description of the test structure and first experimental results

The contact end resistor (CER) shown in fig. 9 consists of four terminals, two of which, not in diagonal position, are used for forcing the current through the contact area, whereas the other two are used for voltage monitoring. This particular test device was applied for the first time by Cohen et al. [58] in the characterization of Al–Si on n^+ - and p^+ -Si, and subsequently, by the same authors, in the study of PtSi contacts as a function of the doping level in Si shallow junctions [34]. The contact resistivity was derived in a straightforward way from

$$\rho_c = (V/I)A, \quad (5.1)$$

where A is the contact area.

Two sets of experiments were performed. In part of the samples Pt was deposited at room temperature after dipping the Si surface in HF solution immediately before the deposition. In this case ρ_c was found to range between 19 and $105 \times 10^{-8} \Omega \text{ cm}^2$ on p^+ -Si, and from 22 to $85 \times 10^{-8} \Omega \text{ cm}^2$ on n^+ -Si. A clear shift in ρ_c was in fact detected by increasing the implant dose. In the second set of experiments, the wafers underwent sputter etching before and in situ heating during Pt deposition. An improvement by a factor of 2 for the contacts on p^+ -Si, and by a factor of 6 for the contacts on n^+ -Si was observed.

Despite these results, however, the procedure followed by the authors to derive the contact resistivity is quite questionable [88]. In fact, in this type of test structure, the measured parameter is the contact end resistance. Therefore, the relation holding between resistance and contact resistivity, in the ideal case of diffusion width equal to contact window width, is eq. (3.8), as determined in section 3.1, relative to the TLTR.

Chern and Oldham [60] used first eq. (3.8) in order to extract ρ_c values from a CER structure similar to fig. 9. From the measured end resistances they extracted contact resistivity values independent of the contact length, as can be expected when 2-D effects are negligible.

However, when the transmission length l_t is small compared to the geometrical features of the test structure, two-dimensional effects have to be taken into account.

5.2. Two-dimensional current flow

The parasitic effect on the CER structure due to the diffusion overlap in real contacts was first examined by Armstrong and Stribley [101], and later investigated in more detail by Swirhun et al. [25]. To measure the extent of the effect, in ref. [25] test structures with varying W , d and δ have been fabricated in silicon and polysilicon. Results were reported for three different fabrication runs. In the wafers labeled as “CLS” the diffusion regions were formed by low-dose As^+ implantation ($R_{sh} = 22.8 \text{ } \Omega/\square$) and contacts consisted of $\text{Al}/\text{W}/\text{Pd}_2\text{Si}$. The wafers labeled as “Ply” had contacts on n^+ -polysilicon ($\text{Al}/\text{W}/\text{PtSi}$ for Ply24 and Al/W for Ply13, with $R_{sh} = 10.9$ and $57 \text{ } \Omega/\square$ for the respective diffusion layers). Wafers labeled “Bst” were fabricated to measure ρ_c for $\text{Al}/\text{W}/\text{PtSi}$ contacts to shallow B diffusions. Again, the film thicknesses were chosen sufficiently low not to affect appreciably R_{sk} during silicidation.

It was shown that, for very large overlap, the measured resistance in Ply24, Ply13 and Bst samples, is proportional to the diffusion sheet resistance, but insensitive to the component of resistance due to the metal–semiconductor contact. For good contacts to high sheet resistance diffusions the parasitic component can be as much as three orders of magnitude higher than the ideal 1-D contact end resistance. Therefore, for any $\delta \neq 0$, the use of eq. (3.8) will lead to a large overestimation of ρ_c . Similar effects were found in ref. [102] where a 2-D model based on the finite-element method was used to simulate $\text{Al}/\text{Ti}/n^+\text{-Si}$ contacts.

In analogy to previously reported results for the TLTR and CKR cases, numerical simulations to the measured R_c data, using ρ_c as a parameter, allow an accurate determination of contact resistivity, independent of test geometry and diffusion sheet resistance, as shown by the dashed lines in fig. 35.

5.3. Misalignment effects

To verify the extent of the misalignment on the expected values of end resistance, the CER structure has been simulated in the case of fig. 36, where $\delta_1 \neq \delta_2$, $(\delta_1 + \delta_2)/2 = \delta = 2.5 \text{ } \mu\text{m}$ and the contact area is $A = 5 \times 5 \text{ } \mu\text{m}^2$ [102,103]. The results of the calculations are shown in fig. 37, for δ_1 ranging between 0.5 and $4.5 \text{ } \mu\text{m}$, with $\rho_c = 1 \times 10^{-7} \text{ } \Omega \text{ cm}^2$ and for two different sheet resistances $R_{sh} = R_{sk} = 20$ and $100 \text{ } \Omega/\square$ respectively. It is shown that a perfectly aligned contact produces a minimum in the end resistance. Non-symmetric current crowding tends to increase the end resistance, with more pronounced effects for larger sheet resistance values. In this respect, the misalignment error acts to increase the effective alignment tolerance.

For the two cases shown in fig. 37, an offset of $2 \text{ } \mu\text{m}$ in the contact position would give contact resistivity values of 2.6 and $8 \times 10^{-7} \text{ } \Omega \text{ cm}^2$ for $R_s = 20$ and $100 \text{ } \Omega/\square$ respectively, if symmetric current crowding is assumed. The misalignment error for this geometry is about 70%

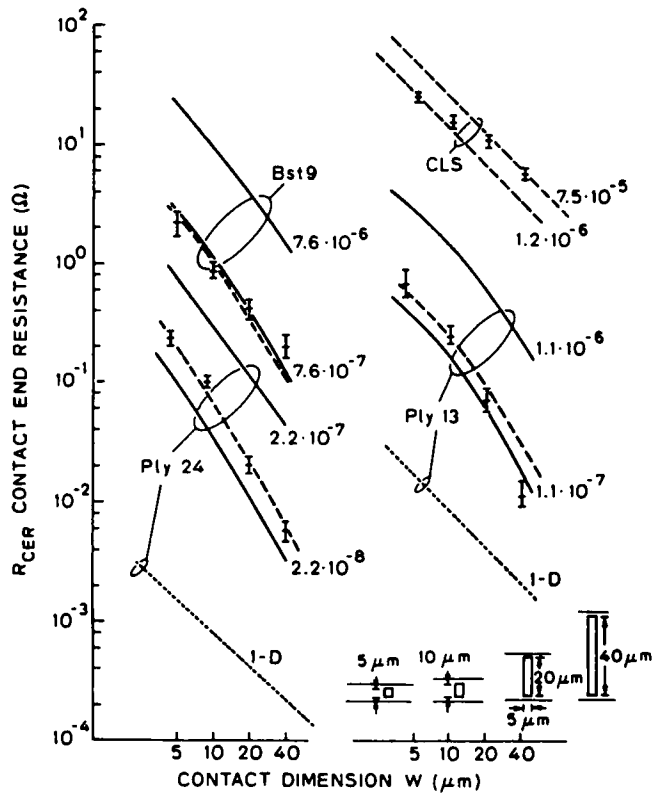


Fig. 35. Measured end resistance as a function of the contact dimension W for structures with $\delta = 2.5 \mu\text{m}$ and $d = 5 \mu\text{m}$. Best-fit curves shown dashed. Simulations that bracket the best fit shown solid. One-dimensional prediction for Ply data sets shown dotted. From ref. [25]. © 198-IEEE.

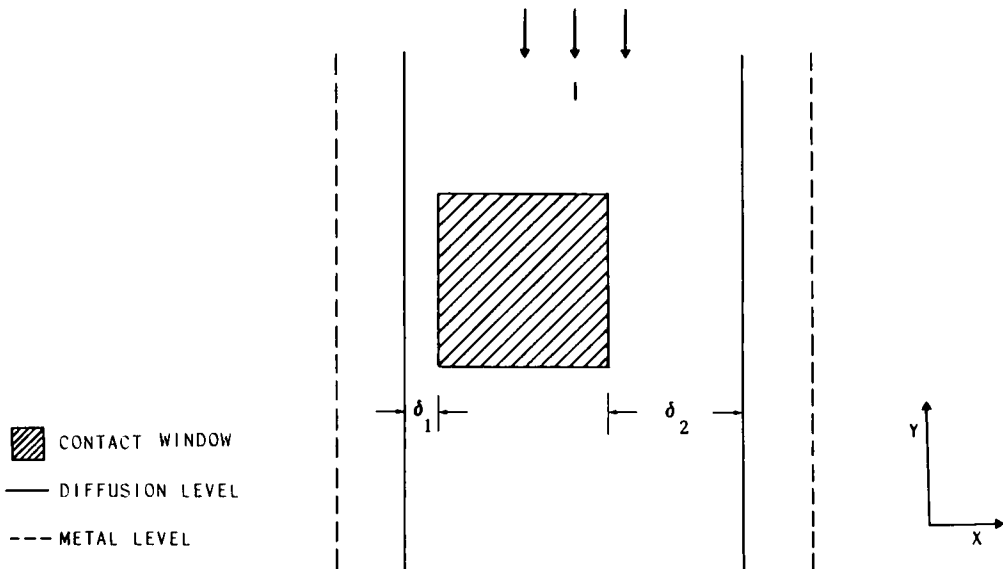


Fig. 36. Misaligned contact window in the CER structure.

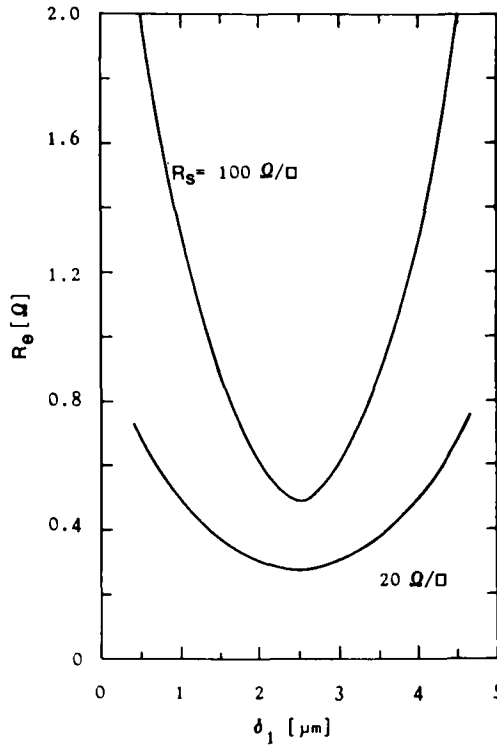


Fig. 37. Calculated end resistance as a function of δ_1 (see fig. 36).

of the corresponding error in the contact resistivity introduced by assuming a simple 1-D current flow and neglecting the crowding effects. Even larger errors would result for smaller contact resistivities.

5.4. Generalized extraction curves and sheet resistance modification effects

Similarly to the TLTR and CKR cases, generalized extraction curves can be derived for the contact end resistor [32,96]. The plots reported in figs. 38a, 38b and 38c refer to the cases $\Omega = 1, 3$ and $1/3$, respectively. As a general comment, it can be underlined again the need to sense very low resistance values, especially when the transmission length is small with respect to the geometrical dimensions of the test pattern. For the sake of completeness, in fig. 38a the theoretical calculations based on the TLM equation (3.8) are also reported (as dots).

6. The six-terminal cross Kelvin resistor

6.1. Description of the test structure

The six-terminal CKR structure shown in fig. 39 allows the direct measurement of both interfacial and end resistance, which is an advantage since it is possible, in principle, to determine at the same time the contact resistivity and sheet resistance underneath the contact.

In refs. [59,94] Al-Si metallizations on phosphorus-doped silicon (with $R_{sh} = 6 \Omega/\square$ and a calculated surface concentration of $1.58 \times 10^{19} \text{ cm}^{-3}$) have been investigated with a six-termi-

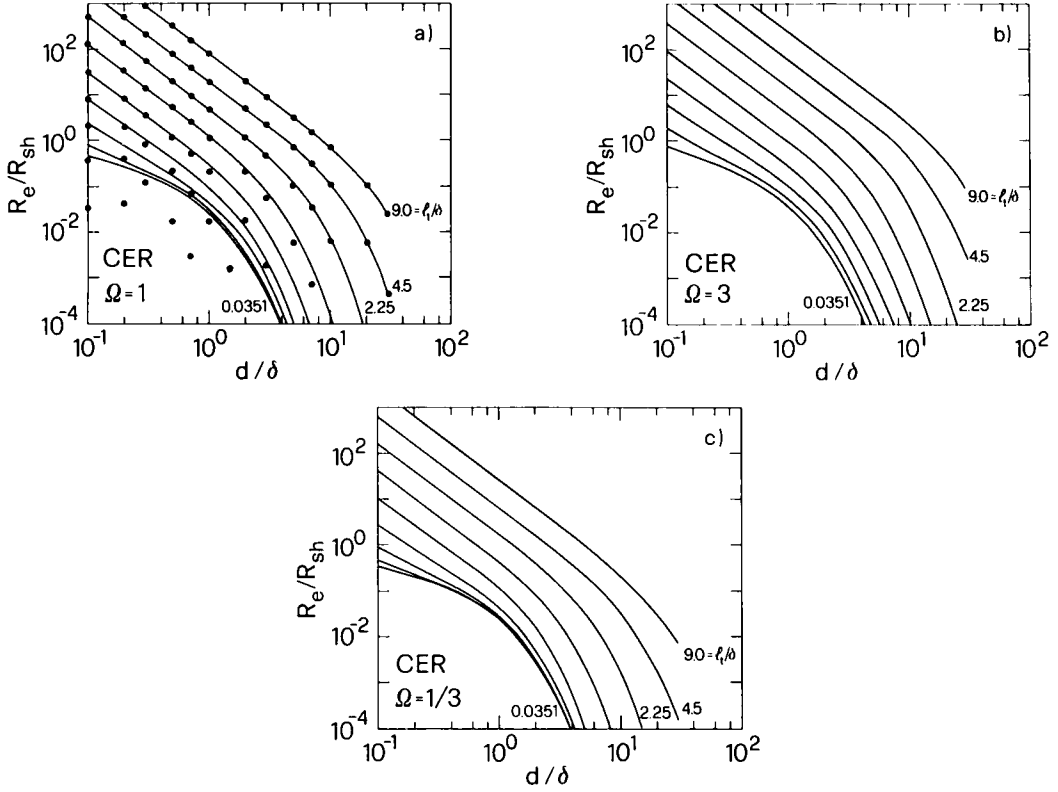


Fig. 38. Generalized extraction curves (solid lines) for a square-contact CER in the cases $\Omega = 1$ (a), 3 (b) and $1/3$ (c). The parameter l_t/δ is in octave steps. For comparison, analytical calculations from eq. (3.8) are reported as dots.

nal resistor. The resulting values of contact resistivity $((1.4\text{--}3.2) \times 10^{-6} \Omega \text{ cm}^2$, depending on the annealing temperature) and sheet resistance under the contact ($5.6\text{--}12.3 \Omega/\square$) were determined by means of the 1-D equations (4.1) and (3.8), respectively. Due to the very high l_t values, these results are not expected to need any correction for 2-D current flow.

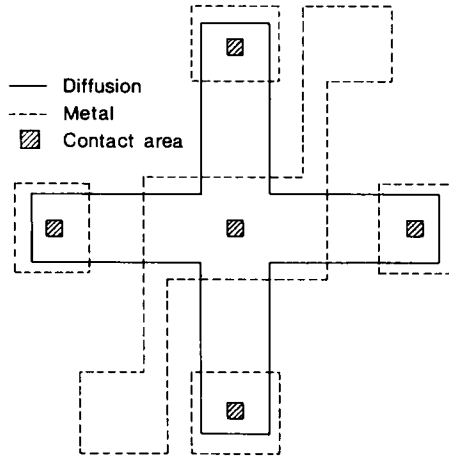


Fig. 39. Conventional six-terminal CKR structure.

6.2. Misalignment effects

The fabrication process used to prepare this type of structure introduces two sources of error in the measurements. The first one is due to the resistive drop occurring as a consequence of the different width of the diffused area and contact window. Then, as observed in the CKR case, the misalignment of the contact window with respect to the diffused tap (fig. 40) could also play a role. Unlike the previous CER structure, in this case the misalignment can occur in both the x and y directions.

The first effect is very similar to the four-terminal case, and will not be discussed further.

Concerning the errors due to the misalignment [93,103], one expects that the contribution to the voltage monitored across the contact increases or decreases such value depending on the relative position of the contact with respect to the diffused tap. Figs. 41a and 41b show the values of contact resistance predicted for different types of contact misalignment with 2-D simulations [103]. The figures refer to the case of an area $A = 5 \times 5 \mu\text{m}^2$, $\delta_1 + \delta_2 = \delta_3 + \delta_4 = 5 \mu\text{m}$, $\rho_c = 1 \times 10^{-7} \Omega \text{ cm}^2$ and $R_{sh} = R_{sk} = 30$ and $100 \Omega/\square$, respectively. In order to avoid the overlapping of the contact windows, which would occur if these were drawn in the same figure for different misalignments, the values of contact resistance have been reported inside squares whose position is related to the different δ_1 and δ_2 assumed in the simulations. In particular, the five squares on the horizontal line, from left to right, correspond to $\delta_1 = 0.5, 1.5, 2.5, 3.5$ and $4.5 \mu\text{m}$, respectively, and the five ones on the vertical line, from bottom to top, refer to δ_2 varying in the same set of values. As expected, in position a) the contact resistance is less affected by the parasitic area than in the perfectly aligned case. In fact, in this case the parasitic resistive drop between the end of the current tap and the leading edge of the contact is minimized. Furthermore, the additional parasitic contribution consisting in the resistive drop between the lateral side of the contact and the voltage tap is also minimized. On the other hand, this second effect becomes more important by moving the contact window in positions b) and c), corresponding to an increasing amount of current flowing laterally.

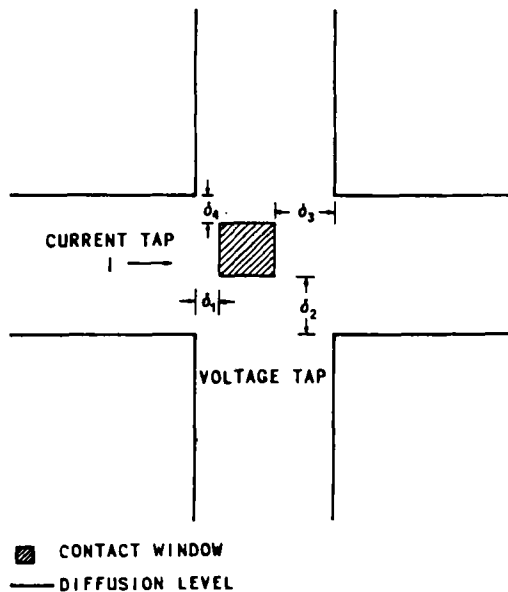


Fig. 40. Example of misaligned contact window in the CKR structure.

It can also be observed that a symmetry line exists, so that the contact resistance assumes identical values for positions of the contact window symmetric with respect to this line. This result can be explained by considering the contact structure as a three-terminal network connected like a two-port. In this case the reciprocity theorem of linear networks holds. Since the interfacial resistance is equal to the transfer impedance of the resistor [103], the current-voltage combinations shown in figs. 42a and 42b are equivalent. On the other hand, because of the geometrical symmetry, the combination shown in fig. 42b is equivalent to that of fig. 42c, confirming the results of the computer simulations reported in fig. 41.

As this point, it would be useful to evaluate the need for accurate measurements of the four geometrical tolerances around the contact and for their use in accurate simulations of the correct contact geometry. Is it absolutely necessary? Or, is it sufficiently accurate to determine experimentally a misalignment-corrected value for R_i by averaging the interfacial resistance obtained by permutation of the current and voltage lines, as suggested in ref. [59]? In this last case one can assume that the contact window is perfectly aligned, and then apply the corresponding simulation model using a value of tolerance δ equal to the average of the δ_i . To see the extent of the error by following this procedure, the application of this method has been simulated to the contact window in position c) of figs. 41a and 41b. From this point of view,

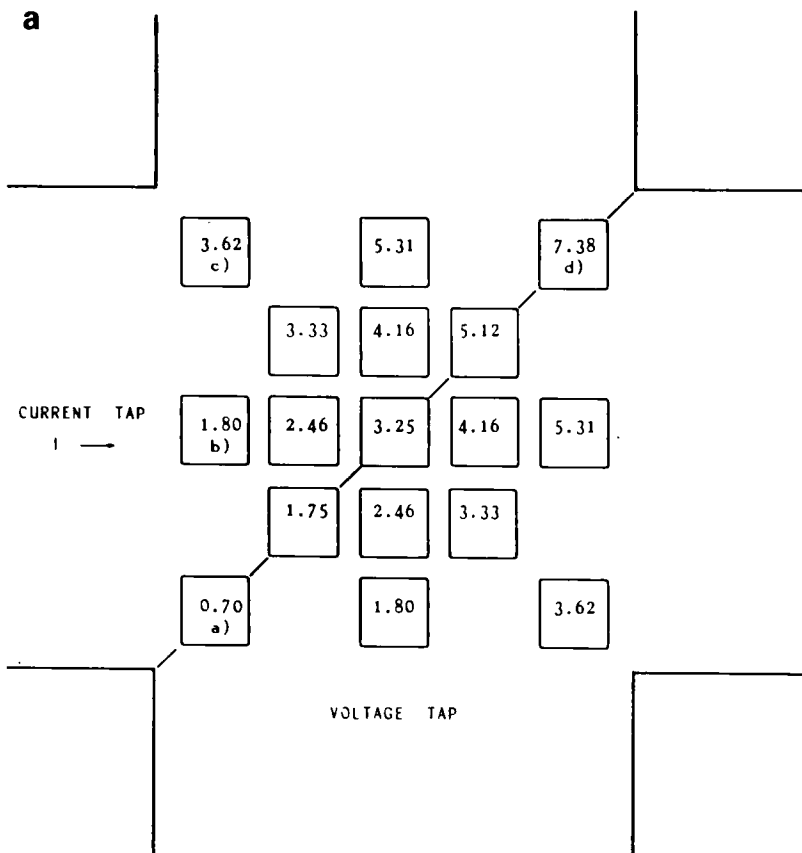


Fig. 41. Contact resistance simulation showing the misalignment effect in the case of $R_s = 30 \Omega/\square$ (a) and $100 \Omega/\square$ (b). See text for details. From ref. [103]. © 198-IEEE.

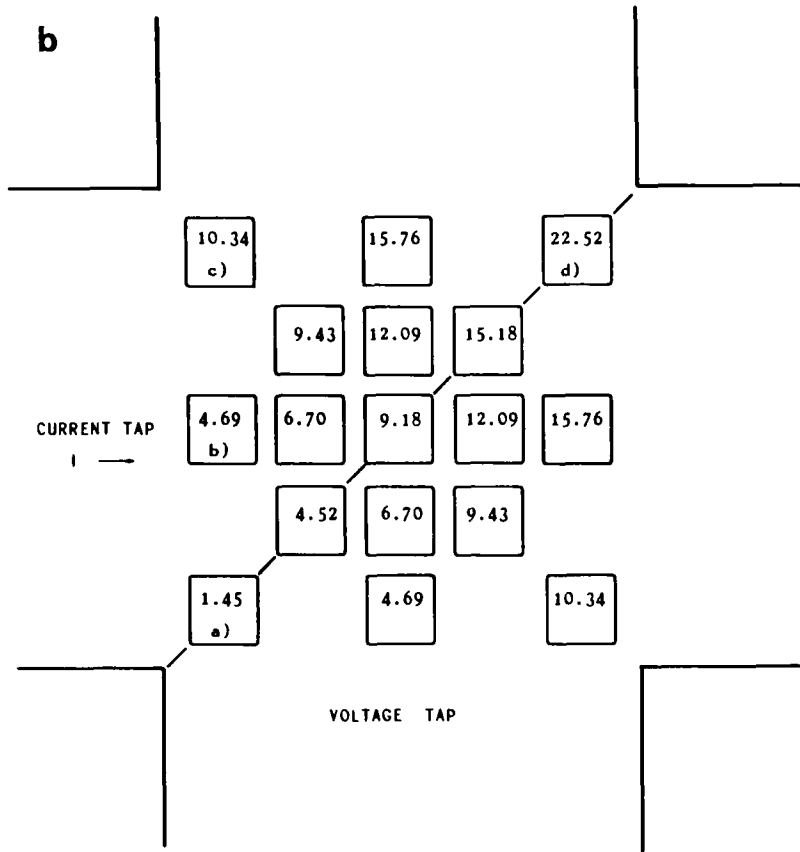


Fig. 41 (continued).

the four corner positions are obviously equivalent to each other. The results are reported in table 5 for two different values of contact size, tolerance, contact resistivity and sheet resistance. For comparison, both the perfectly aligned and the misaligned cases are shown. The following observations can then be derived.

Table 5

Contact area A (μm^2)	Tolerance δ (μm)	ρ_c ($\Omega\text{ cm}^2$)	R_s (Ω/\square)	Aligned contact R_i (Ω)	Misaligned contact	
					R_i^+ a) (Ω)	ρ_c^+ b) ($\Omega\text{ cm}^2$)
5×5	2.5	1×10^{-7}	100	9.18	11.2	4.2×10^{-7}
		1×10^{-8}	100	7.59	9.68	1.9×10^{-7}
2×2	1.5	1×10^{-7}	30	6.74	7.28	1.2×10^{-7}
		1×10^{-7}	100	15.87	17.71	1.6×10^{-7}
		1×10^{-8}	100	11.94	13.87	4.6×10^{-7}

a) Misalignment-corrected value as derived following ref. [59].

b) Contact resistivity as extracted from R_i^+ considering a perfectly aligned contact window.

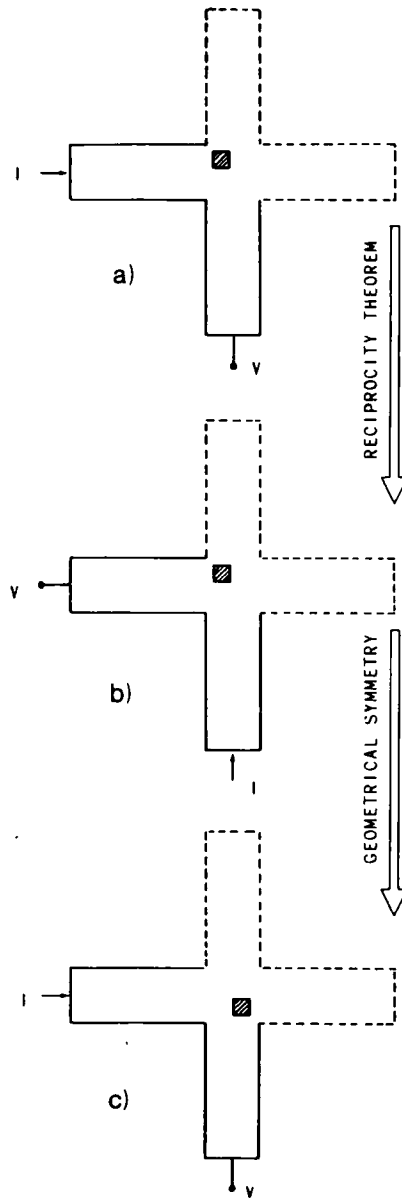


Fig. 42. Equivalent current-voltage combinations in misaligned contacts. From ref. [103]. © 198-IEEE.

(1) The averaging method is certainly effective in reducing the misalignment error in the determination of the contact resistance. In the worst case ($R_s = 100 \, \Omega/\square$ and $\rho_c = 1 \times 10^{-8} \, \Omega \, \text{cm}^2$) the misalignment-corrected value R_i^+ is only 28% higher than the corresponding R_i value expected for a perfectly aligned $5 \times 5 \, \mu\text{m}^2$ contact.

(2) However, significant errors can still occur when deriving the contact resistivity from the misalignment-corrected R_i^+ since the increase in contact resistance is attributed only to a higher value of ρ_c .

(3) The accuracy of the averaging method is sensibly improved by using shrinked test geometries, as observed even in the most unfavorable case of $\rho_c = 1 \times 10^{-8} \Omega \text{ cm}^2$ and $R_s = 100 \Omega/\square$.

7. New test structures

New test structures have recently been proposed in the literature for the extraction of the contact resistivity from suitable electrical measurements.

Lei et al. [104] proposed a vertical, six-terminal test structure in which the contact resistivity can be directly extracted by means of the 1-D formula (4.1). They concluded that the vertical test structure gives a more linear relation between contact resistance and contact area than the six-terminal test structure.

In ref. [105], Loh et al. introduced the so-called sidewall resistor, a structure very similar to fig. 4 realized with polycrystalline silicon etched anisotropically with plasma etchers to define a mesa island. Contact resistivities as low as $(7.2\text{--}7.6) \times 10^{-8} \Omega \text{ cm}^2$ were extracted, with a resolution of $5 \times 10^{-9} \Omega \text{ cm}^2$.

A TLM-like tester was suggested by Ng [106], created in a regular MOSFET with local shorts created in the gate oxide of the gate-to-drain overlap region. For self-aligned silicided structures, a resolution of $\rho_c \leq 10^{-8} \Omega \text{ cm}^2$ can be achieved.

Other structures have been proposed, more directly related to the planar structures discussed above. They will be discussed in more detail in sections 7.1–7.3.

7.1. The self-aligned contact end resistor (SCER)

The SCER is presented in fig. 43. This test pattern has been used for the characterization of Al/CoSi₂/n⁺-Si contacts [74,102,107]. Three self-aligned resistors were prepared, with a contact length $d = 2 \mu\text{m}$ and three different contact widths of 2, 5 and 10 μm , respectively. The contact length was restricted to 2 μm because for longer contacts the end resistance becomes vanishingly small, making its accurate determination difficult [102]. The data obtained from end resistance measurement are shown in fig. 44 as a function of the contact width. They are consistent with the 1-D equation (3.8), and a single value of contact resistivity ($\rho_c = (4.5 \pm 1) \times 10^{-7} \Omega \text{ cm}^2$) can be derived for the three different contact geometries used. In this case, $R_{sk} = 43 \Omega/\square$ was determined on a separate plain wafer prepared by following the same technological processes as for the test structures.

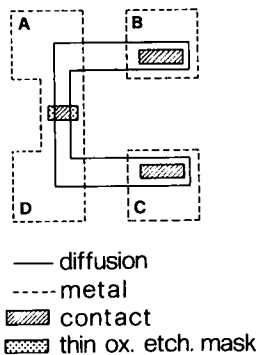


Fig. 43. Self-aligned contact end resistor (SCER).

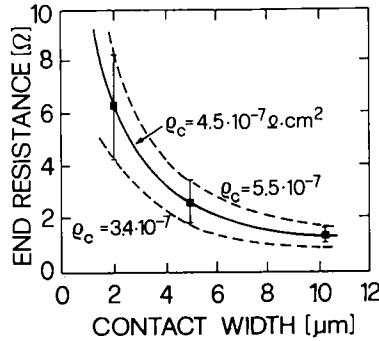


Fig. 44. Experimental results of end resistance as a function of the contact width in a SCER. The solid line is obtained from eq. (3.8) for $\rho_c = 4.5 \times 10^{-7} \Omega \text{ cm}^2$ and $R_{sk} = 43 \Omega/\square$. The dashed lines have been calculated so as to bracket the experimental errors. From ref. [107]. © 198-IEEE.

The computation of the contact resistivity reported above does not take into account the current crowding in the lateral dopant diffusion X_{jl} . However, it can be shown [107] that the two-dimensional current distribution can be neglected, at least for $X_{jl} \leq 2000 \text{ \AA}$ and for a contact resistivity on the order of $10^{-7} \Omega \text{ cm}^2$.

7.2. The self-aligned six-terminal cross Kelvin resistor (SKR)

With a simple three-mask process, a self-aligned six-terminal cross Kelvin resistor was obtained [107], in which the diffusion tap to contact overlap is reduced to the lateral diffusion of the dopant (fig. 45). The preparation procedure is such that the shape of the test contact is rectangular regardless of its size, while the contact dimensions are equal to the widths of the diffused stripes reduced by twice the lateral diffusion.

Fig. 46 reports the logarithm of the measured contact resistance versus the logarithm of the contact area, for 12 different contact areas realized on the same test chip, in the case of an Al/TiSi₂/n⁺-Si metallization scheme [108]. The data exhibit a linear behaviour with a slope

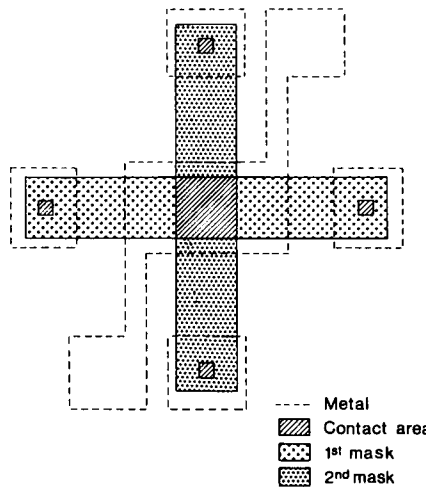


Fig. 45. The self-aligned six-terminal cross Kelvin resistor (SKR).

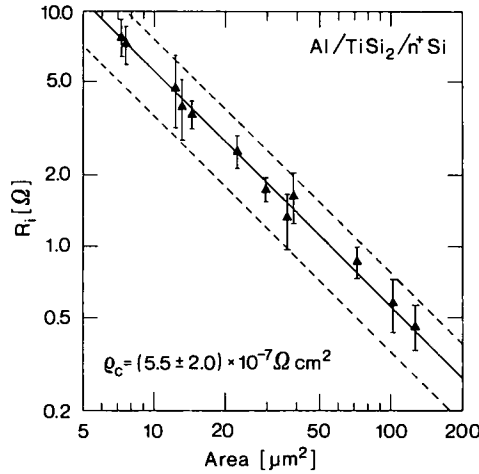


Fig. 46. Experimental results of contact resistance as a function of 12 different contact areas, for Al/TiSi₂/n⁺-Si contacts. The theoretical 1-D slope of -1 (solid line) is verified.

equal to -1 , in agreement with the 1-D model. The contact resistivity value obtained from the intercept of the least-squares regression line is $(5.5 \pm 2) \times 10^{-7} \Omega \text{ cm}^2$. The results indicate that in this type of structure and for values of contact resistivity of this order of magnitude, parasitic effects related to the lateral dopant diffusion and to the doped arms at right angles with respect to the current stripe are completely negligible, so that the corresponding 1-D model [57] can be applied. These conclusions were also theoretically confirmed using the computer model described in section 3.2 [107].

7.3. The circular resistor (CR)

A novel structure, the circular resistor (CR, see fig. 47) has been proposed [109] for extracting values of metal/semiconductor contact resistivity in the case of zero metal sheet resistance. A closed-form, two-dimensional analytical solution of eqs. (2.11) and (2.12), with proper boundary conditions, has been demonstrated, in the form

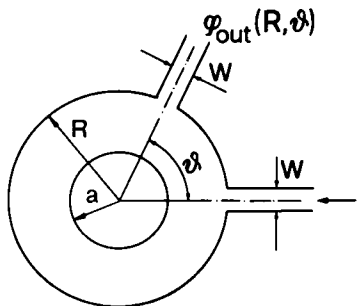


Fig. 47. The circular resistor (CR) with two taps.

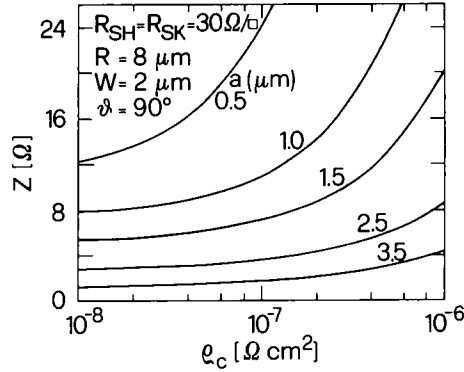


Fig. 48. Resistance in a CR as a function of ρ_c with the radius a as a parameter. The curves refer to $R = 8 \mu\text{m}$, $W = 2 \mu\text{m}$, $R_{sh} = R_{sk} = 30 \Omega/\square$.

$$\frac{Z(\vartheta)}{R_{sh}} = \frac{1}{\pi} \left(\frac{\Omega}{2\alpha a} \frac{I_0(\alpha a)}{I_1(\alpha a)} - \frac{1}{2} \ln p + \sum_{n=1}^{\infty} \frac{\cos(n\vartheta) \sin(n\vartheta_0)}{n^2 \vartheta_0} (1 + 2E_n) \right), \quad (7.1)$$

where Z is the ratio between the voltage φ measured at the end of a stripe (fig. 47) and the current introduced in the other stripe (forming an angle ϑ with the first one), $\alpha = 1/l_t$, a and R the internal and external radii, respectively, $2\vartheta_0$ the angle seen by the stripe with respect to the centre of the structure, and

$$E_n = \frac{\Omega - k_n}{(k_n + \Omega)p^{-n} + (k_n - \Omega)p^n}, \quad p = \frac{a}{R}, \quad k_n = \alpha a \frac{I_{n-1}(\alpha a) + I_{n+1}(\alpha a)}{2nI_n(\alpha a)},$$

where I_n is the Bessel function of imaginary argument.

The CR is shown to work well if the width of the taps is negligible with respect to $2\pi R$, so that it does not affect the potential distribution of the structure. Fig. 48 shows the resistance of the structure calculated for usual geometries and sheet resistance, as a function of the contact resistivity. As for the CKR, this structure shows best resolution for small contact radius.

8. Contact resistance in VLSI contacts

8.1. Contact resistance and scaling

It is well known that the VLSI goal is the increase of the number of devices per chip by decreasing the feature size of the technological process. In order to know in advance the electrical behaviour of a shrunk device the so-called “scaling rules” have been developed [110,111]. In the case of a constant supply voltage [111] the scaling rules foresee an increase of a factor ℓ in the currents of the devices, where ℓ is the scaling factor. If the contact area scales as ℓ^2 , one could argue that the current density at the contacts increases as ℓ^3 [112]. This conclusion is incorrect, because it does not take into account the current crowding effect. Suppose, e.g., to reduce the length of a contact with constant technological parameters (ρ_c , R_{sh} and R_{sk}). If the 1-D model is valid and if, at the beginning, the contact is “electrically long”,

the front resistance remains fixed at the constant value $Z = \rho_c / wl_t$ until $d \approx l_t$. In this case the current crowding and the local current density remain approximately unchanged. Then, if the contact width is reduced too, the current density increases “just” by a factor $\ell \times \ell = \ell^2$.

Moreover, if the 2-D current flow is taken into account, the reduced contact geometry has, as a counterpart, the beneficial effect of the two lateral sides of the contact available for the conduction of the current. A quantitative confirmation of this conclusion can be extracted from fig. 15: for small values of l_t/δ , with $\delta = \text{constant}$, a sublinear behaviour can be detected for the front resistance as a function of the contact size.

For what we have seen until now, the most stressed zones of a contact are the edge regions, especially for small values of the transfer length. Particularly, the corner zones of a rectangular-shaped contact must bear very high current densities, as can be seen by means of proper 2-D simulations. Then, in order to minimize electromigration effects it is strongly recommended to round the corners of micron-sized contacts. Anyway, in most cases, a beneficial (but often unwanted) rounding effect is routinely produced in the photolithographic steps of VLSI contacts, thus minimizing this “hot spot” effect.

8.2. Contact resistivity and reliability

Several papers in the past have underlined the need for high dopant concentrations at the silicon/metal interface, in order to decrease the corresponding values of contact resistivity. The effect of a low contact resistivity on contact reliability has been taken into account only in refs. [112–116] where it was shown that the resulting current crowding underneath the contact can give rise to concerns because of the particularly elevated current density at the contact leading edge. In fact, it is well known that the median time to failure (MTF) of a contact is related to the current density across the contact through the relationship:

$$\text{MTF} = AJ^{-n} \exp(E_a/k_B T), \quad (8.1)$$

where E_a is the activation energy of the prevailing transport mechanism, k_B the Boltzmann constant, J the current density and the value of n is typically in the range 1–6 depending on the current density. We have used the 2-D simulation program to calculate the current density distribution in a contact of $1 \times 1 \mu\text{m}^2$, with a tolerance $\delta = 0.5 \mu\text{m}$, as a function of the contact resistivity. The average current density in the length $\Delta x = 0.1 \mu\text{m}$ has then been calculated for different values of the contact resistivity and substituted into eq. (8.1) to derive the corresponding values of MTF. In fig. 49 are reported the resulting values of contact resistance and MTF as a function of the contact resistivity. The determination of MTF was performed by assuming $n = 1$ and $n = 2$. This represents an optimistic prediction since most of the calculated current densities would imply a higher current coefficient. From fig. 49 it can be seen that a decrease in contact resistivity from 1×10^{-6} to $1 \times 10^{-7} \Omega \text{ cm}^2$ is accompanied by a substantial decrease in contact resistance, whereas the corresponding MTF decreases. On the other hand, if values of ρ_c in the range 10^{-8} – $10^{-7} \Omega \text{ cm}^2$ are obtained, the corresponding contact resistance does not change appreciably, while the corresponding MTF is lowered by almost an order of magnitude.

Of course one could argue that the contact requirements to avoid electromigration become considerably relaxed once refractory metals or compounds (such as, e.g., W or TiN) are incorporated in metallization schemes [112,114]. Furthermore the model is quite far from being rigorous, since temperature effects related to different Joule contributions, as a function of ρ_c ,

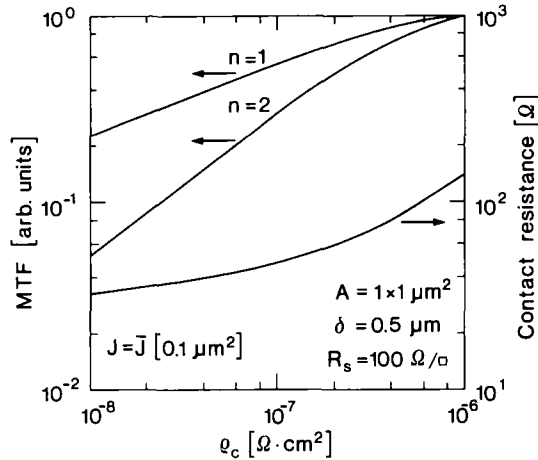


Fig. 49. Calculated median time to failure (MTF) and contact resistance as a function of the contact resistivity for a $1 \times 1 \mu\text{m}^2$ terminal contact of a device, with alignment tolerance $\delta = 0.5 \mu\text{m}$ and $R_{sh} = R_{sk} = 100 \Omega/\square$.

are not considered. As a conclusion, we would like to point out that, based on previous considerations, a potential problem exists as far as electromigration is concerned, and the effect of an excessively low ρ_c on the enhancement of the contact failure rate should be better kept in mind.

9. Conclusions

In this paper we have examined the most widely used experimental methods for the extraction of the contact resistivity from contact resistance measurements. Generalized extraction curves are given for each test structure, in order to bypass tedious and time-consuming two-dimensional simulations. Analytical models are also reviewed and compared to computer simulations. A considerable amount of experimental results on the most common metal/semiconductor structures are reported, and related to the original test pattern used. Finally, the impact of the very large scale integration on the reliability of low-resistivity ohmic contacts has been briefly discussed.

Acknowledgements

The authors wish to thank Professor S.S. Lau for his encouragement. They are also indebted to Dr. I. Suni, Dr. P. Cappelletti, Professor G. Soncini and Dr. P. Ostojia for fruitful discussions, to Messrs. P. Negrini, S. Guerri and G. Pizzochero for sample preparation and to Dr. G. Cardinali and Dr. M. Impronta for valuable help in the computational work. The permission of Dr. R. Gillenwater, Professor S.S. Lau, Dr. U. Lienweg, Dr. L.W. Linholm, Professor M.-A. Nicolet, Dr. G.K. Reeves, Professor K.C. Saraswat and Dr. S.M. Sze to reproduce their figures is acknowledged with gratitude. Thanks are also due to the American Institute of Physics, Elsevier Editorial Services, the Institute of Electrical and Electronic Engineering and Pergamon Press. This work was partially supported by the European Economic Community under the ESPRIT project, Contract 554, and by the Italian National

Research Council under the Progetto Finalizzato Materiali e Dispositivi per l'Elettronica a Stato Solido.

References

- [1] A.Y.C. Yu, *Solid State Electron.* 13 (1970) 239.
- [2] C.Y. Chang, Y.K. Fang and S.M. Sze, *Solid State Electron.* 14 (1971) 541.
- [3] E.H. Rhoderick, *Metal-Semiconductor Contacts* (Oxford Univ. Press, Oxford, 1978).
- [4] W.J. Boudville and T.C. McGill, *J. Vacuum Sci. Technol.* B3 (1985) 1192.
- [5] T. Sebestyen, *Solid State Electron.* 25 (1982) 543.
- [6] G.Y. Robinson, *Solid State Electron.* 18 (1975) 331.
- [7] E. Yamaguchi, T. Nishioka and Y. Ohmachi, *Solid State Electron.* 24 (1981) 263.
- [8] A. Callegari, E.T.-S. Pan and M. Murakami, *Appl. Phys. Letters* 46 (1985) 1141.
- [9] F. Lønnum and J.S. Johannessen, *Electron. Letters* 22 (1986) 632.
- [10] J. Bardeen, *Phys. Rev.* 71 (1947) 717.
- [11] A.M. Cowley and S.M. Sze, *J. Appl. Phys.* 96 (1965) 3212.
- [12] L.J. Brillson, *Phys. Rev. Letters* 40 (1978) 260.
- [13] J.M. Woodall and J.L. Freeouf, *J. Vacuum Sci. Technol.* 19 (1981) 794.
- [14] J.M. Woodall, J.L. Freeouf, G.D. Pettit, T. Jackson and P. Kirchner, *J. Vacuum Sci. Technol.* 19 (1981) 626.
- [15] D.C. Marvin, N.A. Ives and M.S. Leung, *J. Appl. Phys.* 58 (1985) 2659.
- [16] M.A. Rao, E.J. Caine, S.I. Long and H. Kroemer, *IEEE Electron Device Letters* EDL-8 (1978) 30.
- [17] D. Krillow and Y. Chung, *Appl. Phys. Letters* 51 (1987) 846.
- [18] L.A. Farrow, C.Y. Sandroff and C. Tamargo, *Appl. Phys. Letters* 51 (1987) 1931.
- [19] M.-A. Nicolet, *Thin Solid Films* 52 (1978) 415.
- [20] M. Mäenpää, I. Suni, M.-A. Nicolet, F. Ho and P. Iles, *Proceedings of the 15th IEEE Photovoltaic Specialists Conference* (1981) p. 518.
- [21] M. Finetti, I. Suni and M.-A. Nicolet, *Solar Cells* 9 (1983) 179.
- [22] M. Finetti, I. Suni, M. Bartur, T. Banwell and M.-A. Nicolet, *Solid State Electron.* 27 (1984) 617.
- [23] A. Shepela, *Solid State Electron.* 16 (1973) 477.
- [24] J.M. Aitken and C.Y. Ting, *IEEE IEDM Tech. Digest* (1981) 50.
- [25] S.E. Swirhun, W.M. Loh, R.M. Swanson and K.C. Saraswat, *IEEE Electron Device Letters* EDL-6 (1985) 639.
- [26] J. Ohdomari, M. Hori, T. Maeda, A. Ogura, H. Kwarada, T. Hamamoto, K. Sano, K.N. Tu, M. Wittmer, J. Kimura and K. Yoneda, *J. Appl. Phys.* 54 (1983) 4679.
- [27] C.J. Kircher, *Solid State Electron.* 14 (1971) 507.
- [28] M. Finetti, S. Guerri, P. Negrini and A. Scorzoni, *Thin Solid Films* 130 (1985) 37.
- [29] M. Finetti, A. Scorzoni and I. Suni, *Vide* 42 (1987) 99.
- [30] S.E. Swirhun, K.C. Saraswat and R.M. Swanson, *IEEE Electron Device Letters* EDL-5 (1984) 209.
- [31] W.M. Loh, S.E. Swirhun, E. Crabbé, K.C. Saraswat and R.M. Swanson, *IEEE Electron Device Letters* EDL-6 (1985) 441.
- [32] W.M. Loh, S.E. Swirhun, T.A. Schreyer, R.M. Swanson and K.C. Saraswat, *IEEE Trans. Electron Devices* ED-34 (1987) 512.
- [33] C.Y. Ting and M. Wittmer, *Thin Solid Films* 96 (1982) 327.
- [34] S.S. Cohen, P.A. Piacente, G. Gildenblat and D.M. Brown, *J. Appl. Phys.* 53 (1982) 8856.
- [35] R.M. Anderson and T.M. Reith, *J. Electrochem. Soc.* 122 (1975) 1337.
- [36] H. Muta, *Japan. J. Appl. Phys.* 17 (1978) 1089.
- [37] D.L. Meier and P. Rai-Choudhuri, *Proceedings of the Electrochemical Society Spring Meeting, San Francisco, CA, May 1983*, p. 611.
- [38] J. Hui, S. Wong and J. Moll, *IEEE Electron Device Letters* EDL-6 (1985) 479.
- [39] L. van den Hove, R. Wolters, K. Maex, R.F. de Keersmaecker and G.J. Declerck, *IEEE Trans. Electron Devices* ED-34 (1987) 554.
- [40] T. Banwell, M.-A. Nicolet and D.M. Scott, *Thin Solid Films* 107 (1983) 67.
- [41] M. Wittmer and T.E. Seidel, *J. Appl. Phys.* 49 (1978) 5827.
- [42] J.B. Bindell, W.M. Moller and E.F. Labuda, *IEEE Trans. Electron Devices* ED-27 (1980) 420.
- [43] M. Wittmer, C.Y. Ting, I. Ohdomari and K.N. Tu, *J. Appl. Phys.* 53 (1982) 6781.
- [44] I. Ohdomari, K. Suguro, M. Akijama, T. Maeda, K.N. Tu, I. Kimura and K. Yoneda, *Thin Solid Films* 89 (1982) 349.

- [45] K. Maex, L. van den Hove, R.F. de Keersmaecker, A. Perio, J.C. Oberlin, J. Torres, G. Bomchil and W. van der Weg, *Vide* 42 (1987) 95.
- [46] P. Zwicknagl, S.D. Mukherjee, P.M. Capani, H. Lee, H.T. Griem, L. Rathbun, J.D. Berry, W.L. Jones and L.F. Eastman, *J. Vacuum Sci. Technol.* B4 (1986) 476.
- [47] A. Ketterson, F. Ponce, T. Henderson, J. Klem and H. Morkoç, *J. Appl. Phys.* 57 (1985) 2305.
- [48] W.P. Hong, K.S. Seo, P.K. Bhattacharya and H. Lee, *IEEE Electron Device Letters* EDL-7 (1986) 320.
- [49] V.L. Rideout, *Thin Solid Films* 48 (1978) 261.
- [50] N. Braslau, *J. Vacuum Sci. Technol.* 19 (1981) 803.
- [51] A. Piotrowska, A. Guivarc'h and G. Pelous, *Solid State Electron.* 26 (1983) 179.
- [52] N. Braslau, *J. Vacuum Sci. Technol.* A4 (1986) 3085.
- [53] H.H. Berger, *J. Electrochem. Soc.* 119 (1972) 507.
- [54] H.H. Berger, *Solid State Electron.* 15 (1972) 145.
- [55] W. Kellner, *Siemens Forsch. Entwicklungsber.* 4 (1975) 137.
- [56] G.K. Reeves, *Solid State Electron.* 23 (1980) 487.
- [57] S.J. Proctor and L.W. Linholm, *IEEE Electron Device Letters* EDL-3 (1982) 294.
- [58] S.S. Cohen, G. Gildenblat, M. Ghezzi and D.M. Brown, *J. Electrochem. Soc.* 129 (1982) 1335.
- [59] S.J. Proctor, L.W. Linholm and J.A. Mazer, *IEEE Trans. Electron Devices* ED-30 (1983) 1535.
- [60] J. Chern and W.G. Oldham, *IEEE Electron Device Letters* EDL-5 (1984) 178.
- [61] W.M. Loh, K.C. Saraswat and R.W. Dutton, *IEEE Electron Device Letters* EDL-6 (1985) 105.
- [62] W.M. Loh, S.E. Swirhun, T.A. Schreyer, K.C. Saraswat and R.M. Swanson, *IEEE IEDM Tech. Digest* (1985) 586.
- [63] A. Scorzoni and M. Finetti, *IEEE Trans. Electron Devices* ED-35 (1988) 386.
- [64] S.B. Schuldt, *Solid State Electron.* 21 (1978) 715.
- [65] E.G. Woelk, H. Krautle and H. Beneking, *IEEE Trans. Electron Devices* ED-33 (1986) 19.
- [66] W. Shockley, Report No. AI-TOR-64-207, Air Force Atomic Laboratory, Wright-Patterson Air Force Base, Ohio (1964).
- [67] H. Murrmann and D. Widmann, *Solid State Electron.* 12 (1969) 879.
- [68] H. Murrmann and D. Widmann, *IEEE Trans. Electron Devices* ED-16 (1969) 1022.
- [69] I.F. Chang, *J. Electrochem. Soc.* 117 (1970) 368.
- [70] G.K. Reeves and H.B. Harrison, *IEEE Electron Device Letters* EDL-3 (1982) 111.
- [71] C.Y. Ting and C.Y. Chen, *Solid State Electron.* 14 (1971) 433.
- [72] H.M. Naguib and L.H. Hobbs, *J. Electrochem. Soc.* 124 (1977) 573.
- [73] M. Finetti, A. Scorzoni and G. Soncini, *IEEE Electron Device Letters* EDL-5 (1984) 524.
- [74] A. Scorzoni, M. Finetti, G. Soncini and I. Suni, *Alta Freq.* 61 (1987) 341.
- [75] M. Finetti, P. Ostojia, S. Solmi and G. Soncini, *Solid State Electron.* 23 (1980) 255.
- [76] M. Finetti, S. Solmi and G. Soncini, *Solid State Electron.* 24 (1981) 539.
- [77] G.S. Marlow and M.B. Das, *Solid State Electron.* 25 (1982) 91.
- [78] M. Finetti, I. Suni and M.-A. Nicolet, *Solid State Electron.* 26 (1983) 1065.
- [79] B. Kovács and I. Mojzes, *IEEE Trans. Electron Devices* ED-33 (1986) 1041.
- [80] D.B. Scott, W.R. Hunter and H. Shichijo, *IEEE Trans. Electron Devices* ED-29 (1982) 651.
- [81] T. Hara, H. Suzuki, M. Furukawa and K. Amemiya, *Japan. J. Appl. Phys.* 22 (1983) L340.
- [82] E.D. Marshall, W.X. Chen, C.S. Wu and S.S. Lau, *Appl. Phys. Letters* 47 (1985) 298.
- [83] M. Finetti, E.T.-S. Pan, I. Suni and M.-A. Nicolet, *Appl. Phys. Letters* 42 (1983) 987.
- [84] G.K. Reeves, *Solid State Electron.* 23 (1980) 487.
- [85] H.P. Kattelus, J.L. Tandon and M.-A. Nicolet, *Solid State Electron.* 29 (1986) 903.
- [86] G. McNeil, in: *Ohmic Contacts to Semiconductors*, Proceedings of the 134th National Meeting of the Electrochemical Society, Montreal, 6–11 October 1969, ed. B. Schwartz, p. 305.
- [87] K.K. Shih and J.M. Blum, *Solid State Electron.* 15 (1972) 1177.
- [88] A. Scorzoni, M. Finetti and G. Soncini, *Alta Freq.* 53 (1984) 282.
- [89] M. Finetti, S. Guerri, P. Negrini, A. Scorzoni and I. Suni, *Sixth International Conference on Thin Films*, Stockholm, August 1984.
- [90] R.L. Maddox, *IEEE Trans. Electron Devices* ED-32 (1985) 682.
- [91] J.M. Ford, *IEEE Trans. Electron Devices* ED-32 (1985) 840.
- [92] R.L. Gillenwater, M.J. Hafich and G.Y. Robinson, *IEEE Electron Device Letters* EDL-7 (1986) 674.
- [93] R.L. Gillenwater, M.J. Hafich and G.Y. Robinson, *IEEE Trans. Electron Devices* ED-34 (1987) 537.
- [94] J.A. Mazer, L.W. Linholm and A.N. Saxena, *J. Electrochem. Soc.* 132 (1985) 440.
- [95] M. Finetti, A. Scorzoni and G. Soncini, *IEEE Electron Device Letters* EDL-6 (1985) 184.

- [96] A. Scorzoni, unpublished results.
- [97] S.A. Chalmers and B.G. Streetman, IEEE Trans. Electron Devices ED-34 (1987) 2023.
- [98] U. Lienweg and D.J. Hannaman, IEEE Electron Device Letters EDL-8 (1987) 202.
- [99] T.A. Schreyer and K.C. Saraswat, IEEE Electron Device Letters EDL-7 (1986) 661.
- [100] A. Scorzoni and U. Lienweg, to be published.
- [101] N.P. Armstrong and K.R. Stribley, Proceedings of the 2nd International IEEE VLSI Multilevel Interconnection Conference, Santa Clara, CA (1985) p. 389.
- [102] I. Suni, M. Finetti and K. Grahm, MRS Spring Meeting, Palo Alto, CA (1986).
- [103] A. Scorzoni, M. Finetti, K. Grahm, I. Suni and P. Cappelletti, IEEE Trans. Electron Devices ED-34 (1987) 525.
- [104] T.F. Lei, L.Y. Leu and C.L. Lee, IEEE Electron Device Letters EDL-7 (1986) 259.
- [105] W.M. Loh, P.J. Wright, T.A. Schreyer, S.E. Swirhun, K.C. Saraswat and J.D. Meindl, IEEE Electron Device Letters EDL-7 (1986) 477.
- [106] K.K. Ng, IEEE Trans. Electron Devices ED-34 (1987) 544.
- [107] P. Cappelletti, M. Finetti, A. Scorzoni, I. Suni, N. Circelli and G. Dalla Libera, IEEE Trans. Electron Devices ED-34 (1987) 532.
- [108] M. Finetti and A. Scorzoni, unpublished results.
- [109] A. Scorzoni and M. Vanzi, to be published.
- [110] R.H. Dennard, F.H. Gaensslen, H.-N. Yu, V.L. Rideout, E. Bassous and A.R. LeBlanc, IEEE J. Solid State Circuits SC-9 (1974) 256.
- [111] P.K. Chatterjee, W.R. Hunter, T.C. Holloway and Y.T. Lin, IEEE Electron Device Letters EDL-1 (1980) 220.
- [112] P.A. Gargini, C. Tseng and M.H. Woods, IEEE IRPS Proc. (1982) p. 66.
- [113] S. Vaidya and A.K. Sinha, IEEE IRPS Proc. (1982) p. 50.
- [114] S. Vaidya, R.H. Schutz and A.K. Sinha, J. Appl. Phys. 55 (1984) 3514.
- [115] J.G.J. Chern, W.G. Oldham and N. Cheung, IEEE Trans. Electron Devices ED-32 (1985) 1341.
- [116] J.G.J. Chern, W.G. Oldham and N. Cheung, IEEE Trans. Electron Devices ED-33 (1986) 1256.